INVESTIGATION OF QUASI-PERIODIC NOISE FEATURES IN X-PERSEI

A THESIS SUBMITTED TO
THE GRADUATE SCHOOL OF NATURAL AND APPLIED SCIENCES
OF
MIDDLE EAST TECHNICAL UNIVERSITY

BY

ZEYNEP ACUNER

IN PARTIAL FULFILLMENT OF THE REQUIREMENTS
FOR
THE DEGREE OF MASTER OF SCIENCE
IN
PHYSICS

MAY 2014

Approval of the thesis:

INVESTIGATION OF QUASI-PERIODIC NOISE FEATURES IN X-PERSEI

submitted by **ZEYNEP ACUNER** in partial fulfillment of the requirements for the degree of **Master of Science in Physics Department, Middle East Technical University** by,

Prof. Dr. Canan Özgen _____
Dean, Graduate School of **Natural and Applied Sciences**

Prof. Dr. Mehmet T. Zeyrek _____
Head of Department, **Physics**

Prof. Dr. Altan Baykal _____
Supervisor, **Physics Department, METU**

Examining Committee Members:

Prof. Dr. Nilgün Kızıloğlu
Physics Dept., METU _____

Prof. Dr. Altan Baykal
Physics Dept., METU _____

Prof. Dr. Şölen Balman
Physics Dept., METU _____

Assoc. Prof. Dr. S. Kaan Yerli
Physics Dept., METU _____

Assoc. Prof. Dr. S. Çağdaş İnam
Electrical and Electronics Eng. Dept., Başkent University _____

Date: _____

I hereby declare that all information in this document has been obtained and presented in accordance with academic rules and ethical conduct. I also declare that, as required by these rules and conduct, I have fully cited and referenced all material and results that are not original to this work.

Name, Last Name: ZEYNEP ACUNER

Signature :

ABSTRACT

INVESTIGATION OF QUASI-PERIODIC NOISE FEATURES IN X-PERSEI

Acuner, Zeynep
M.S., Department of Physics
Supervisor : Prof. Dr. Altan Baykal

May 2014, 93 pages

In this thesis, timing and spectral properties of the Be type X-ray binary X-Persei based on Rossi X-Ray Timing Explorer (RXTE) have been presented.

Results of the power spectral analysis of RTXE data show QPO features detected between $\sim$ 0.1-0.4 Hz which are reported for the first time. Another significant property of X-Per's power spectra is the time dependent excess that can be observed between 0.01-0.08 Hz throughout the observations. These power excesses are interpreted as an inherent feature of source's accretion. Besides this, hardness properties of the source have been carefully examined, which gives an insight to the QPO generation process. It has been concluded that QPO generation is most efficient during time intervals with soft photon abundance where highest QPO frequencies are observed (3-7/7-10 keV).

Although X-Per's general accretion pattern is that of wind accretion which matches with the predictions of Quasi-Spherical Acretion Theory, these investigations also imply the existence of an accretion disk that exists throught the

RXTE observations around the pulsar 4U 0352+309. Values estimated for inner Keplerian radius and magnetic field hence the magnetospheric radius clearly indicate that the accretion disk and the magnetic field closely interact which can be considered as the source of aperiodic variability.

Keywords: Quasi-periodic oscillations, accretion powered pulsars, neutron stars, accretion disks, X-Persei

ÖZ

X-PERSEİ'DEKİ PERİYODİK BENZERİ GÜRÜLTÜ YAPILARININ İNCELENMESİ

Acuner, Zeynep
Yüksek Lisans, Fizik Bölümü
Tez Yöneticisi : Prof. Dr. Altan Baykal

Mayıs 2014 , 93 sayfa

Bu tezde X-ışını ışınımı yapan Be tipi bir çiftli yıldız olan X-Persei'nin Rossi X-Ray Timing Explorer (RXTE) uydusundan alınan verilerle belirlenen zamanlama ve tayfsal özellikleri sunulmuştur.

Güç tayflarının incelenmesi ile elde edilen sonuçlara göre, kaynak 0.1-0.4 Hz frekans aralığında periyodik benzeri salınımlar göstermektedir. Kaynağın güç tayflarının bir başka özelliği ise 0.01-0.08 Hz arasında görülen zamana bağlı frekans değiştiren güç fazlalığıdır. Bu tayfsal özellik X-Per'in kütle aktarımının içsel bir özelliği olarak yorumlanmıştır. Bunun yanında kaynağın X-ışını ışınım sertliği de zamana bağlı incelenmiştir. Bu incelemeye göre QPO üretiminin en verimli olduğu enerji aralığı 3-7/7-10 keV'a denk gelmektedir.

X-Per'in kütle aktarım özellikleri, Küresel-Benzeri Aktarım Teorisi'nin öngörülerine uygun olmakla birlikte RXTE verilerinin kapsadığı zaman aralığında bir

aktarım diskinin varlığını da desteklemektedir. Hesaplanan Kepler diskinin iç yarıçapı, manyetik alan ve manyetosferik yarıçap değerleri, olası aktarım diskinin ve atarcanın manyetik alanının etkileştiğini ve gözlenen periyodik benzeri salınımların kaynağının bu etkileşim olabileceğini göstermektedir.

Anahtar Kelimeler: Periyodik benzeri salınımlar, aktarım güçlü atarcalar, nötron yıldızları, aktarım diskleri, X-Persei

ACKNOWLEDGMENTS

I would like to express my sincere gratitudes to Prof. Dr. Altan Baykal for his supervision, guidance, advice and insights throughout this research. I would also like to thank Assoc. Prof. Dr. S. Çağdaş İnam, especially for his guidance on the discussion of observational findings. I am grateful to receive Prof. Dr. Şölen Balman's valuable advice on various subjects related to this thesis. I thank Prof. Dr. Jean Swank for her reviews related to timing studies and her useful suggestions on these issues.

I would like to thank my colleagues at METU Astrophysics Group for useful discussions and for their help at all levels of this tedious work. My deep gratitudes are to M. Miraç Serim for his great help, advice and insights related to data analysis and interpretation. It would be harder to reach to a conclusion without his tireless efforts to help solve countless problems that have emerged throughout this thesis. I would also like to thank Şeyda Şahiner for her time, assistance and constructive criticism on this work. My special thanks are due to Dr. Eray Özkural for sharing his insights on the interpretation of results as well as his advice on computational and statistical methods.

I would like to thank all my friends for their support. I owe my deepest gratitudes to my parents for their love, whom have always respected and supported the choices I made throughout my life.

I acknowledge the scholarship from The Scientific and Technological Research Council of Turkey (TUBITAK) through the research project TBAG 109T748.

TABLE OF CONTENTS

APPENDICES

LIST OF TABLES

TABLES

LIST OF FIGURES

FIGURES

CHAPTER 1

INTRODUCTION

The possibility of the existence of neutron stars first came to be with the discovery of the neutrons by Chadwick in 1930s. Afterwards, one of the first ideas regarding their formation was proposed in the work of Baade and Zwicky in 1934, whom foreseen the likelihood of neutron stars' birth in supernova explosions. In the following years, Oppenheimer and Volkoff carried out the primary calculations of neutron star mass and radii. However, the first observational evidence of a rotation powered pulsar hasn't come until 1967, when Bell detected radio pulsations from outside the solar system which later was understood to be the first detection of a pulsar by the humankind. Following this ground breaking discovery, tens of other pulsating radio sources were found across the sky without much delay, with the efforts of astronomers from all around the world whom turned their attention to these new intriguing objects. These important observational findings were published in a few seminal papers, leading to a vast number of theoretical work between 1970 and 1980 which were on the internal structures, surface properties, origin and evolution of neutron stars.

X-ray astronomy, which will later be a crucial part of the study of neutron star binaries, started with the detection of the first extrasolar X-ray source, Sco X-1 (Giacconi et al. 1962). In 1967, a model describing the accretion of Scorpius X-1 was developed by Shklovsky (Shklovsky 1967) that emanated from the observation of an optical counterpart for this object and soon after became the corner stone of the theory of accretion-powered X-ray pulsars. This standard model of accreting X-ray binaries was based on the matter flow from the optical

companion onto the neutron star. After the launch of NASA's first X-ray observatory Uhuru, first pulsating X-ray source, Cen X-3, was observed (Giacconi et al. 1971). With the detection of pulsations from eclipsing binaries Cen X-3 and later, Her X-1 (Tananbaum et al.1972), theoretical assumptions regarding X-ray pulsating neutron stars were deemed to be true. Although the suspicion on the neutron star's existence was lifted when the first radio pulsating neutron star was discovered, sources pulsating in X-rays opened a new window for research regarding pulsars and defined a new group of objects that gain their emission power through accretion from their companions (Ghosh 2007). The subsequent X-ray missions after Uhuru such as Ariel V, SAS 3, HEAO 1, Einstein, Tenma, EXOSAT, Ginga, ROSAT, RXTE, BeppoSAX, IXAE, XMM-Newton, Chandra and INTEGRAL have deepened the knowledge on X-ray pulsars and as of 2012, the number of sources exhibiting X-ray pulsations are beyond 400 (Caballero et al. 2012).

X-ray luminosity emitted from accreting X-ray binaries result from the conversion of the gravitational energy of accreted matter into kinetic energy. As the matter falls down onto the large gravitational potential well of the compact object, it gains tremendous acceleration. However, when it meets with the neutron star it is abruptly slowed down, giving away its kinetic energy mostly in X-rays while freely falling. This process is so energetic that most of the time these sources appear to be the brightest objects in the X-ray sky. Hereafter, these X-ray binaries are referred to as accretion-powered pulsars and is the main interest of this thesis (Ghosh 2007).

CHAPTER 2

X-RAY BINARIES

2.1 Main Characteristics of Accretion Powered X-ray Pulsars

Accreting X-ray pulsars have a wide range of pulsation frequencies varying from as short as $\sim$2 milliseconds to as long as 10^4 seconds. Existence of detectable pulsations as well as the long range of periods enables one to identify these compact objects as neutron stars, rather than white dwarfs or black holes (Ghosh 2007).

X$-$ray binaries are divided in two as low-mass (LMXB) and high-mass (HMXB) X-ray binaries, according to the mass and hence, the spectral type of the donor star. Division is established in accordance with the nature of the optical companion which determines the nature of the mass transfer and the environment inside the binary around the compact object (Reig 2011).

2.2 LMXBs

Low mass X-ray binaries have optical companions with masses of $M < 1M_{\odot}$ and spectral type later than. These systems also have low magnetic fields. Milky Way and Magellanic Clouds have a total of 187 LMXRBs in (Liu et al.2005,2006,2007). In the first case, during later stages of its evolution, donor star in the binary expands and fills its Roche lobe. Roche lobe is defined as the equipotential surface around a star in which the matter is gravitationally bound to that star. Therefore, matter remaining outside the Roche lobe is not

controlled by the pull of the optical companion and is accreted onto the compact object through the inner Lagrangian point. Material transferring via Roche lobe overflow has rather high angular momentum so it cannot be accreted directly onto the compact object. Instead, an accretion disk forms where inflowing matter loses its energy gradually before finally meeting up with the star and getting bounded to the stellar magnetic field lines. This matter is then carried onto the neutron star hot spots by the field lines where its energy is transformed into X−ray radiation.

2.3 HMXBs

High mass X−ray binaries have younger optical companions with O or B spectral types which have masses greater than $5M_{\odot}$. These systems have high magnetic fields reaching B $\sim 10^{12}$ G. There are 114 HMXBs in our Galaxy and 128 HMXBs in the Magellanic Clouds (Liu et al.2005,2006,2007). Stellar wind accretion takes place when the donor star is a massive O or B type star capable of producing very strong stellar winds with mass loss rate $M \sim 10^{-4} - 10^{-6} M_{\odot}$ per year. In these binary systems, orbital separation is not larger than one stellar radius, so

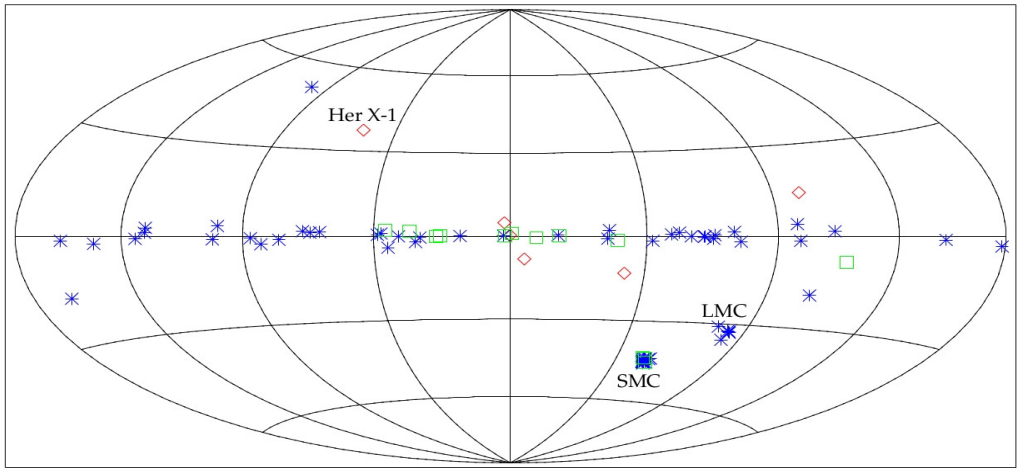

Figure 2.1: Distribution of accretion powered pulsars in the Milky Way Galaxy (Ghosh 2007). Asterisks refer to pulsars in HMXBs and diamonds refer to pulsars in LMXBs while squares are pulsars with uncertain binary classifications.

that the compact object stays in the zone that is occupied by stellar wind of the optical companion. Here, however, the flow is not too energetic and infalling matter can directly be accreted onto the neutron star (Caballero et al. 2012). HMXBs are divided in two subgroups as, BeXRB (transient and persistent) and SGXB (disc fed,wind fed,SFXT).

2.3.1 SGXBs

Due to their bright and persistent emission in X−rays, SGXBs were the first kind of HMXRBs to be discovered. For a long time, until the discovery of BeXRBs, they were thought to be the standard and abundant type of HMXRBs. In these sources, stellar wind of the donor is significant, reaching up to 10^{-6} to 10^{-8} $M_{\odot}$/yr with terminal velocities of about 2000 km/s. With the existence of a compact object nearby to accrete some of the stellar wind material, this wind can generate and fuel a bright X-ray binary. Accretion is also possible via Roche Lobe Overflow and the formation of an accretion disk is to be expected. There

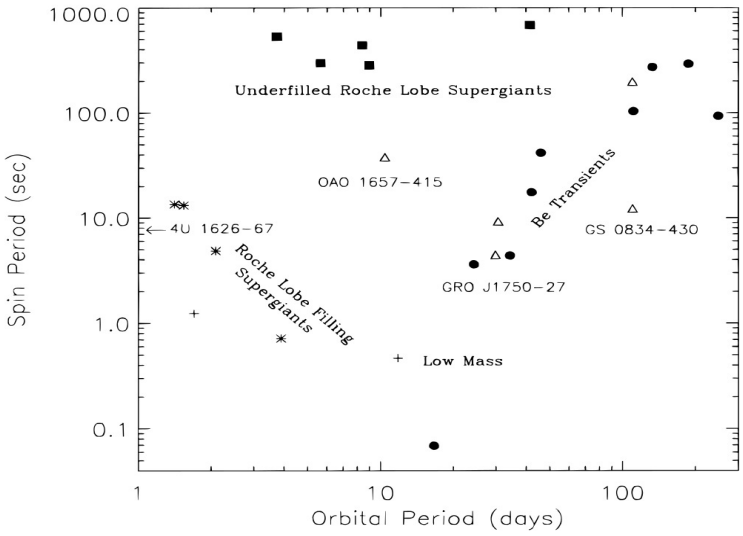

Figure 2.2: Corbet Diagram. P_{spin} versus $P_{orbital}$ plot for accretion powered pulsars. Asterisks refer to Roche lobe filling SGXBs while squares are SGXBs that underfill their Roche lobe. Circles refer to BeXRBs, pluses to LMXBs and triangles to binary pulsars with unknown type (Bildsten et al. 1997).

are both wind and disk fed SGXRBs detected in and outside the Milky Way (Reig 2011).

2.3.2 BeXRBs

Be type X-ray binaries have Oe or Be type dwarf, subgiant or giant star (non-supergiant) fast rotators with a luminosity class of III, IV or V and a compact object, possibly a neutron star. The existence of a white dwarf BeXRB is shown to be probable yet have not been observed to date, due to the long quiescence times predicted for these systems. On the other hand, a recent discovery of the first black hole-Be type star binary provides strong evidence to the fact that BeXRBs having compact objects other than neutron stars exist (Casares et al. 2014). Especially when they are in outburst, BeXRBs appear as the brightest objects in the X−ray sky.

Donor stars in these systems take the prescript "e" after their spectral class notation because they exhibit emission lines in their spectra. Among the various lines observed, such as He and Fe, the well-known ones are of Hydrogen,namely Balmer and Paschen lines. The spectra of Be stars have one more characteristic feature, which is their increased infrared emission compared to the normal B type stars with absorption lines. This feature is known as the infrared excess. Reason of these spectral differences in Be stars is considered to be the existence of an equatorial circumstellar disk. Instead of feeding from an accretion disk, the accreting pulsar in a BeXRB is powered by the strong stellar wind of its optical companion and/or its optical companion's decretion disk. This decretion disk is formed by accumulation of the individual mass ejecta from OB star. Although there is no solid theory that has been agreed upon, a common consideration is that the main reason for formation of such a disk is the fast rotation of the Be type stars. On the average, this class of stars have larger observed rotational velocities than B type stars.

Specification of a certain rotational velocity is important in explaining the formation of the circumstellar disk. If this rotational velocity is large enough, centrifugal forces are balanced with Newtonian gravitational forces, resulting in

Table2.1: Statistics regarding X-ray binaries in Milky Way Galaxy (Reig 2011).

Number of neutron-star X-ray binaries[1]	327
Number of suspected HMXB[1]	131
Number of suspected BeXB[2]	63
Number of *confirmed* BeXB[3]	28

[1] Liu et al. (2006) and Liu et al. (2007)

[2] Raguzava & Popov (2007), online version

[3] Reig (2011)

the reduction of equatorial gravity. The suppression of equatorial gravity makes it easy for weak processes such as gas pressure and/or non-radial pulsations to trigger the ejection of photospheric matter from the star. The ejection being quite energetic and having sufficient angular momentum, spins up to form a Keplerian disk around the equatorial plane of the star. There are many models explaining the physical processes that can cause this matter ejection such as wind−compressed model (Bjorkman and Cassinelli 1993), the magnetically torqued disk model (Brown et al. 2008) and non-radial pulsations (Cranmer 2009, and references therein). Although there are a lot of suggestions on the triggering mechanism, once the disk is formed, behaviour of the disk is well described by the viscous decretion disc model (Lee et al. 1991, Okazaki 2001)(Reig 2011). Emission from the accreting pulsar might be caused by the periodic encounters of the neutron star with this disk, which consists of Type 1 outbursts for Be type XRBs.

In general, BeXRBs have moderate eccentricities with $0.1<e<0.9$ and display transient X-ray emission with luminosity changes of a factor greater than 10, in accordance with transient matter accretion from the equatorial disk of the Be star. There also exists BeXRBs which exhibit persistent yet low luminosity X-ray emission of the order of $L_x \sim 10^{34}$ erg/s varying by up to a factor of ~ 10. It is assumed that slowly rotating pulsars tend to show pulsed emission even during the quiescence states while fast rotating pulsars tend to be transient sources (Okazaki, Neguerula 2001).

In binaries with a Be type star, the circumstellar disk is not always effective as

a means of accretion or not even observable. When a Be star is inside a binary, evolution of decretion disks get affected by the compact companion. Compact objects truncate the viscous circumstellar disk and prevent a steady state disk from forming. This further results in instabilities and could even result in disk loss (Clark et al. 2001). In the case of a truncation, stellar wind accretion is the only option for powering the pulsating accretion-powered neutron star. One strong indication of this truncation is the correlation of the variability of H_α line observed in the spectra of these disks with the orbital period of the system. Since, traditionally it is assumed that Be disks are large enough to reach out and beyond the periastron distance, it is of importance to investigate whether the truncation radius is larger than periastron distance or not, for a better understanding of accretion from the equatorial disk.

When disks of binaries are in consideration, outer radius of the disk (R_{out}) is defined as the radius inside which the viscous torque, T_{vis}, is larger than tidal/resonant torque, T_{res}, so that the disk inside R_{out} can be kept intact via viscous forces. For a classical Shakura-Sunyaev disk, this condition is valid for α values smaller than α_{crit} which is the critical value. In evaluation of the viscous torque, it is assumed that the circumstellar disk is isothermal at $0.5T_{eff}$ with

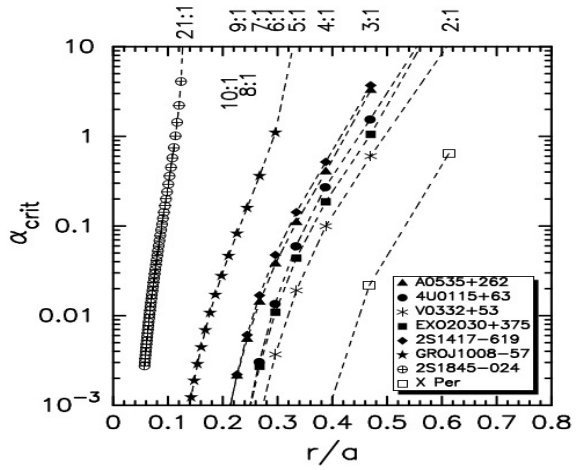

Figure 2.3: Resonance radii values at α_{crit} for eight Be X-ray binary sources (Okazaki and Neguerula 2001). r/a is the ratio of the truncation radius to the periastron distance.

T_{eff} being the effective temperature of the Be star while tidal and resonant torques are averaged over system orbit. An overall look at Figure 2.4 shows that for numerous values of α, the Be disk is truncated at a distance smaller than periastron. This implies that in these systems, neutron star never really encounters the disk and there always remains a gap between the compact object and the optical companion's equatorial disk.

Even in the lack of Type I outbursts, hot massive stars continuously eject matter from their atmospheres. Ejection is accumulated on the disk outer radius, since it cannot go beyond that due to the torques applied by the companion neutron star. After a sufficient amount of accumulation on the disk, it is expected for the disk to go into an unstable state which will be elaborated as the cause of Type II outbursts.

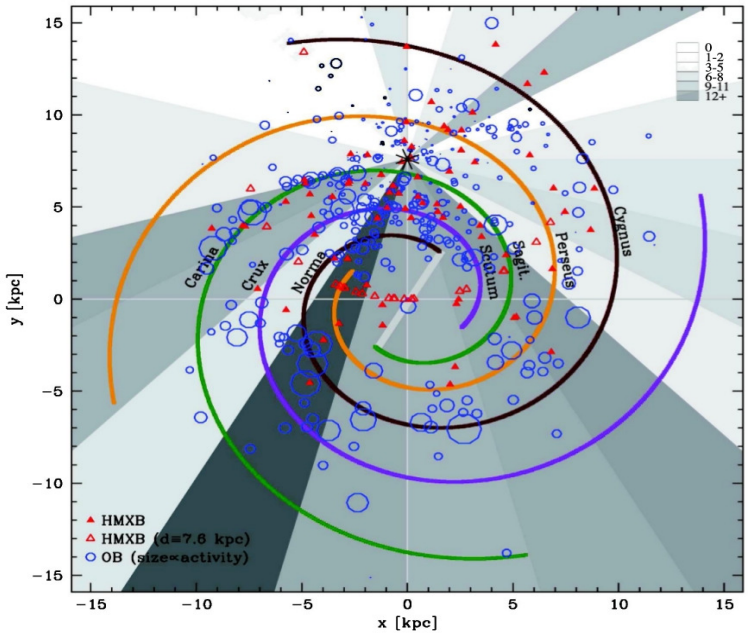

Figure 2.4: Distribution of the HMXBs with known distances (filled triangles), unknown distances (empty triangles) and OB star forming regions (circles with sizes proportional to the activity in the region) in the Milky Way Galaxy (Bodaghee et al. 2010).

Type I Outbursts These outbursts occur with X-ray luminosities between 10^{36}–10^{37} erg/s (<0.2 L_{Edd}) around the time when neutron star and the optical companion are closest, lasting a minimum of several days up to a week, generally amounting to 0.2-0.3 $P_{orbital}$. Here, Eddington luminosity (L_{Edd}) is the luminosity limit that results from the maximum possible mass accretion rate for a compact object after which gravitational and radiation forces cannot balance eachother. This limit is defined as,

$$L_{Edd} = 3.4 \times 10^4 L_{\odot} \left(\frac{M_{star}}{M_{\odot}} \right) \tag{2.1}$$

where $L_{\odot}$ and $M_{\odot}$ are solar luminosity and mass respectively (Ryden 2011).

Clarification on the comparison of the disk size and the periastron distance in BeXRBs come into play in this class of outbursts. Above, it was concluded that the truncated circumstellar disk is smaller than the periastron distance which would normally inhibit accretion. However, this radius is quite close to the Roche radius which is of significance for the accretion phenomenon to take place. For Be binaries that have highly eccentric orbits, the torque on the equatorial disk diminishes as companions drift away from each other which results in a noticeable growth of the disk when far from the periastron point. Matter from this expanded disk flows onto the neutron star when it comes into the periastron during the next orbit. This process causes regular escalations in X−ray luminosity which are designated as Type I or periodical outbursts.

Type II (Giant) Outbursts With luminosities higher than 10^{37} erg/s (around L_{edd}), these outbursts have no correlation with the orbital period. They can be observed to last about several tens of days, covering large intervals in an orbital period and sometimes lasting for more than one cycle of orbit. These outbursts are also associated with the formation of an accretion disk due to the secular spin-up rates and quasi−periodic oscillations observed during the time interval identified with the flare.

Since giant outbursts do not exhibit any kind of orbital modulation, they need to be explained by a different process than that of periodical outbursts. Continuous ejection of matter from Be star regenerates the decretion disk after a period of

disk loss. The disk reforms and expands, as can be inferred from the increased amount of emission coming from it. The steadily growing amount of matter that is supported by the viscous structure gets truncated at the truncation radius due to the torque applied by the neutron star. This truncation adjusts the form of the disk resulting gas accumulation at the outermost regions. Gas build-up at the edges of the circumstellar disk causes the formation of an optically thick region in an otherwise optically thin structure. An optically thick disk is not stable to the effects of radiation−driven warping (Pringle 1996, Porter 1998), hence it commences to precess, getting warped at the same time. Interaction of the warped portion of the disk with the stellar wind and radiation tends to be strong, resulting in a substantial deformation and elongation of these regions. Because of this unstability, ample amounts of gas fall onto the neutron star, inducing a Type II or giant X-ray outburst. After a Type II outburst, decretion disk becomes fainter as it has lost a great deal of its reservoir to the recent outburst.

These sudden rises in X-ray luminosities of X-ray binaries indicate mass accretion rates way higher than the mass loss rates of an ordinary Be type star. However, it should be kept in mind that equatorial disks collect material from their Be companions' winds for years or decades and eject it in an incomparably short time, unlike the timescales valid for periodical outbursts, which explains the seemingly high mass ejection rates (Okazaki, Neguerula 2000). As will be elaborated later in this work, persistent sources showing quite different characteristics than those of transient nature do exist (Reig et al.2013).

2.4 Accretion onto X-ray Binaries

Bright accreting pulsars are observed to have X-ray luminosities $\sim 10^{37}$ ergs/s and these luminosities require accretion rates $\sim 10^{17}$ g/s which corresponds to $10^{-9} M_{\odot}$/yr. O or B type optical companions of compact objects in these binaries are more than sufficient to provide these accretion rates since they readily lose their mass through various processes during their evolution and through the evolution of the binary. These massive stars eject some of their mass as "stellar

winds". Moreover, a subgroup of B spectral class stars known as Be type stars also lose matter to the equatorial disk around them which is another important source of accretion.

Regardless of the accretion process occurring in the binary, matter coming relatively close to the intense magnetic field of the neutron star (ranging from $\sim 10^{11}$ Gauss for an accreting pulsar to as large as 10^{15} Gauss for magnetars), gets channeled by the magnetic field lines towards the magnetic poles. Matter is accreted onto the polar caps, producing two hot spots where the energetic gas clashes onto the surface of the neutron star. Here, funneled matter forms a column-like structure, namely the accretion column or the accretion funnel. When there is an angle between the rotation and magnetic axes of the neutron star, emission emanating from the column is seen as pulsations, modulated by the star's rotation (Ghosh 2007). Accretion in X−ray binaries can happen through one of two main processes. The optical companion of the neutron star in an X−ray binary can either go into a Roche Lobe Overflow or can stay in the Roche Lobe but have strong stellar winds that provide gas flow which starts the accretion onto the compact object.

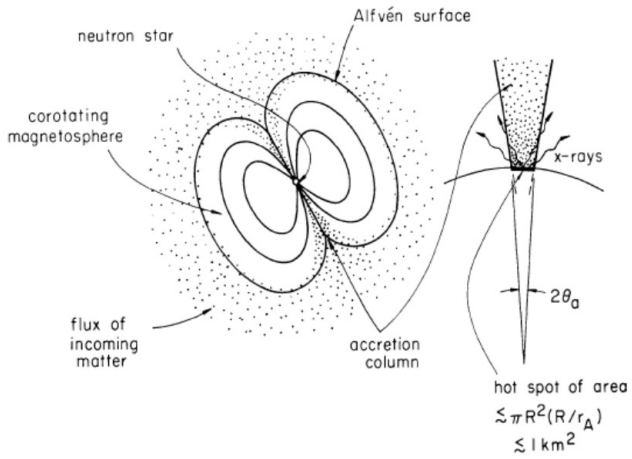

Figure 2.5: Basic model of accretion-powered pulsars describing their general geometry and the hot spot region (Ghosh 2007).

2.4.1 Matter and Angular Momentum Transfer in X-Ray Binaries

X-ray binaries can be powered by either disk or wind accretion when mass transfer is considered as the source of pulsations. These two modes of accretion are determined by the properties of the optical companion.

2.4.2 Accretion via Roche Lobe Overflow

For older binary systems, there has been enough time for the donor star to reach its late evolutionary stages, where the gravitational pressure cannot balance the radiation pressure which is decreased due to the reduction of fusion fuel inside the core of the star. Since these two forces are not in balance anymore, the donor starts to expand. During this stage, star's outer layers remain outside the equipotential surface around it, meaning the loss of matter to its compact companion through the inner Lagrangian point L_1 of the system (Fig. 2.6). This matter, having low radial velocities compared to the azimuthal velocity with respect to the orbiting neutron star, easily gets into an orbit with Keplerian velocity around the gainer. Viscosity of the matter piling up around the compact object is not infinite, which ultimately means the formation of an accretion disk around it due to the spiraling motion of matter under the influence of an immense gravitational field (Nagase 1988).

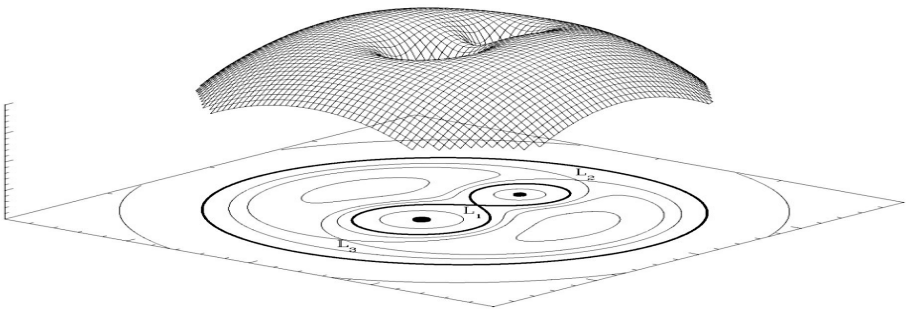

Figure 2.6: 3-D representation of the Roche potential in a binary system with a mass ratio of 2. Lagrangian points L_1, L_2 and L_3 are the locations where gravitational forces cancel out (Van der Sluys, 2014).

The existence of an accretion disk is implied by the high luminosities observed from a large majority of X−ray binaries, especially LMXBs, although it is known that their companions are not massive enough to provide accretion via stellar wind. Another solid evidence is the spin−up trends of these pulsars, which can easily be explained by the accretion disk model. Simply put, this model predicts that a certain torque is applied to the surface of the magnetosphere by the accreted plasma. This phenomenon takes place at the surface where magnetospheric boundary is in contact with the inner edge of the disk at the magnetospheric radius. The magnetospheric or Alfvén radius is given as r_a and is where the pressure emanating from the neutron star's magnetic field equals to the ram and gas pressure of the infalling matter,

$$r_a = \left(\frac{\mu^4}{2GM_x\dot{M}^2}\right)^{1/7} \tag{2.2}$$

$$\simeq 6.8 \times 10^8 cm \left(\frac{\mu}{10^{30}Gcm^3}\right)^{4/7} \left(\frac{10^{-10}M_\odot yr^{-1}}{\dot{M}}\right)^{2/7} \left(\frac{1.4M_\odot}{M_x}\right)^{1/7}. \tag{2.3}$$

where M_x and $\dot{M}$ are the stellar mass and mass accretion rate respectively. μ is the magnetic moment of the star (Bildsten et al. 1997). For a large majority of X−ray pulsars, Alfvén radius is smaller than the corotation radius, r_{co}, which is defined as the point of balance between centrifugal and gravitational forces (Bildsten et al. 1997),

$$r_{co} = \left(\frac{GM_x}{\omega^2}\right)^{1/3}. \tag{2.4}$$

For accretion to occur, magntospheric radius should be smaller than r_{co} and the outcome of this relationship is the fixed accretion torque on pulsars with disk accretion. In the series of seminal papers published by Ghosh and Lamb (1977,1978,1979), the standard accretion disk model of Shakura and Sunyaev is elaborated and a quantitative model of accretion torque is established for the condition that the magnetic and dthe isk axes are aligned. Also, coupling between the neutron star and the disk magnetic fields are discussed in this model in detail.

During the accretion process, matter with sufficient angular momentum goes into the orbit of the neutron star by forming a geometrically thin, $h(r) \gg r$, and optically thick Keplerian accretion disk. Here, the disk has a radial drift

velocity which causes the accretion onto the compact object. The orbital velocity of the plasma is Keplerian,

$$\upsilon = \sqrt{\left(\frac{GM}{R}\right)} \tag{2.5}$$

where G is the gravitational constant, M is the mass of the star and R is the distance to the orbit. In this picture, the disk material is supported against gravity by its rotation alone. Keplerian nature of this structure implies that the matter moving at different velocities at different radii create friction between neighboring layers. This friction is caused by the turbulent and chaotic motions in the disk as well as the small scale magnetic fields, resulting in the loss of angular momentum of disk elements (Shakura & Sunyaev 1973).

However, for this approach to be complete, effects of the magnetic field of the neutron star should be taken into account. For a magnetized neutron star with a dipolar magnetic field and spin perpendicular to the accretion disk, there cannot be a complete screening of the magnetic field from the disk because of three physical processes taking place at the environment of the compact object. These processes have time scales smaller than radial drift time, T_d, of the disk and hence they are effective.

First of all, Kelvin−Helmholtz instability causes the infiltration of stellar magnetic field to disk plasma in a much shorter duration than drift time. Turbulent diffusion is another contributing factor. Large scale convections induced by vertical temperature gradient in the disk results in external magnetic field spreading out through the disk in vertical direction, extending to the center of the disk in a shorter time interval than T_d. The third effect is the recombination of the field lines encircling the disk. Magnetic field lines on top of and beneath the disk continously recombine to the smaller sized fields inside the plasma near the surface. Dominating movements inside the convection cells are differential rotation and circulation, leading to shearing and reconnection of these loops to one another. A combination of these effects eventually causes the magnetic field to penetrate the disk plasma. Threading of the disk by magnetic field results in regions of different properties throughout the disk that has been explained by Ghosh and Lamb in detail. The overall picture of an accreting magnetized neutron star

Table2.2: Regions of accretion flow (Ghosh and Lamb 1979).

Region	Inner Radius	Outer Radius	Length Scale of Change in Physical Variables	Dominant Mechanism of Angular Momentum Transport
Unperturbed disk.....	r_s	Large	r	Effective viscous stress
Outer transition zone.....	r_0	r_s	r	Effective viscous stress
Inner transition zone.....	r_{co}	r_0	$\delta_0 \ll r$	Magnetic stress
Magnetosphere.....	R	r_{co}	r	Magnetic stress

disk is consisted of an unperturbed region where there is no effect of magnetic field (r_s to r_0), a transition region where the plasma is threaded by the stellar magnetic field in between the unperturbed region and the magnetosphere (r_0 to r_{co}) and the magnetosphere itself (r_{co} to R).

In the transition zone, disk plasma moves through the field lines producing currents that results in the screening of the magnetic field which limits the field into a certain screening radius r_s, larger than the corotation radius about an order of $10 - 10^2$. Transition zone is expansive, stretching between r_{co} and r_s. While the transportation of angular momentum is carried out by the effective viscous stresses out in the unperturbed disk region, inside the transition region stellar

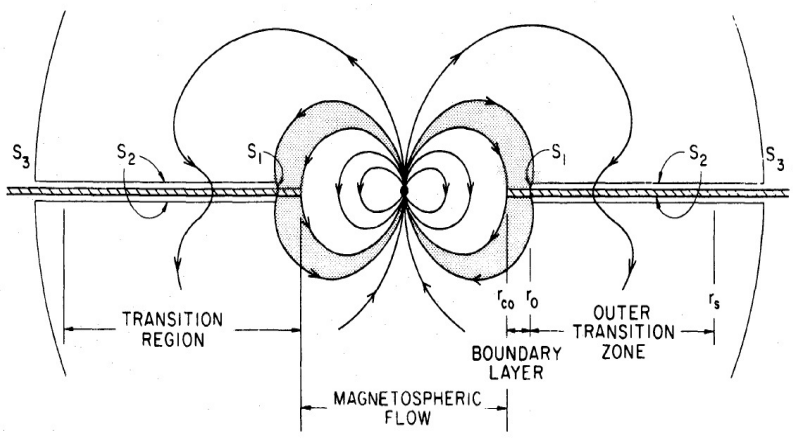

Figure 2.7: Side view of the accretion flow, showing the transition and magnetospheric regions (Ghosh and Lamb 1979).

magnetic field stresses dominate over viscous stresses. Change in the manner of angular velocity transportation separates this region in outer Keplerian and inner non-Keplerian portions aparted by radius r_0, since the angular velocity deviates from Keplerian values as one approaches to the inner parts of the disk. Inside the inner transition zone, Keplerian angular velocity of the infalling plasma decrease to the corototational value because of the magnetic stresses. Magnetic screening by the current circulation is effective and occurs around a factor of 5. It is also inside this region where matter in the disk plane starts to travel vertically alongside the field lines with the effect of magnetic stresses. Causing the rupture of the disk, accretion onto the neutron star proceeds through the so called "accretion bundle". Threaded plasma near the accretion disk still has a considerable amount of cross-field motion. As this bundle approaches star surface, the even more intense magnetic field and the pull of gravitational field reduces the23 cross motion causing the plasma to start a free fall. At the flow alignment radius (r_f), cross field motion of plasma becomes insignificant compared to its field aligned motion. r_f is less than or equal to the Alfvén radius of the neutron star. After this point, plasma gradually approaches the compact object, eventually getting accreted onto it, producing an X-ray emission which determines the accretion luminosity,

$$L_{acc} = \frac{GM_x\dot{M}}{R_x} \simeq 1.2 \times 10^{36} ergs^{-1} \left(\frac{\dot{M}}{10^{-10} M_{\odot} yr^{-1}}\right) \left(\frac{1.4 M\odot}{M_x}\right) \left(\frac{10km}{R_x}\right) \tag{2.6}$$

where R_x is the radius of the neutron star (Bildsten et al. 1997). Apart from the effects of residual magnetic field threading the disk, outer transition zone, consisting of the disk between r_0 and r_s, very much resembles a standard disk. Here, transportation of angular momentum between the disk and the star takes place. Cross field motions appear in this region producing currents that lead to small scale screening of the remaining magnetic field that survived the boundary layer. Screening takes place inside a certain region and mantains the whole magnetic field inside the screening radius coinciding with the outermost edge of the transition zone.

2.4.3 Accretion via Stellar Wind

If the optical companion in an X−ray binary is of early type stars, such as O or B spectral types, strong stellar winds coming from the atmospheres of these massive stars are the main source of accretion. These type of stars are yet to fill their Roche Lobes, however some of their violent atmospheric winds are captured by the intense gravitational field of their compact companions. Amount of matter captured from stellar wind is dependent on the relative velocity of the neutron star as well as the speed of sound at that environment. Neutron star will be able to capture the material in a cylindrical volume of radius R_a which is denoted as the Bondi radius,

$$R_a = \xi \frac{2GM}{\upsilon_0^2} \tag{2.7}$$

with the square of the capture velocity is $\upsilon_0^2 = \upsilon_{orb}^2 + \upsilon_W^2 + c_s^2$ estimated with values of the orbital velocity of the neutron star υ_{orb}, wind velocity with respect to the companion υ_W and the local sound speed c_s (Ghosh and Lamb 1979). In the absence of the formation of an accretion disk, it is expected that the accretion capture radius is larger whereas its shear is expected to be small with stellar magnetic field being enclosed inside of a magnetospheric cavity with radius smaller than R_a. The torque of such an accretion can be estimated from

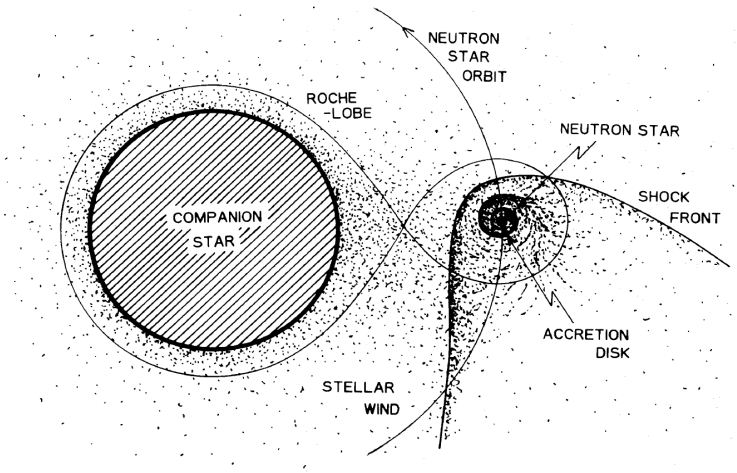

Figure 2.8: An artist's conception of an accretion disk formed in the stellar wind shock (Nagase 1989).

the angular momentum flux across the surface situated at R_a.

$$N = \int_s (-\rho \upsilon_p \omega^2 \Omega + \omega \frac{B_p B_\phi}{4\pi} + \mu \omega^2 \bigtriangledown \Omega).\hat{n} dS \tag{2.8}$$

where ω is the cylindrical radius, υ_p and Ω correspond to the poloidal and angular velocities ofthe plasma. Result of this integration is simply,

$$N = \dot{M} l_a \tag{2.9}$$

Here, stellar wind accretion torque is solely dependent on the mass accretion rate and the specific angular momentum, l_a, of the accreting plasma at R_a (Ghosh & Lamb, 1979). Capture rate of the plasma is the Bondi mass accretion rate,

$$\dot{M} = \pi \rho_W \upsilon_0 R_a^2 \tag{2.10}$$

where ρ_W is density of the wind (Shapiro & Lightman, 1976). The specific angular momentum regarding accreting plasma is,

$$l_a \sim \frac{1}{2} a \upsilon_{orb} \left(\frac{R_a}{a} \right)^2 \tag{2.11}$$

with a being the binary separation where Bondi capture radius is equation (3.6). The final torque expression reads,

$$N = \pi^2 \xi^2 (2GM)^4 \rho_W \upsilon_0^{-7} P_{orb}^{-1} \tag{2.12}$$

Equation of the pulse period change for wind−fed sources dependent on l_a is,

$$-\dot{P} = 3.8 \times 10^{-5} R_6 \left(\frac{M}{M_\odot} \right)^{-1} I_{45}^{-1} \times \left(\frac{l_a}{10^{17} cm^2 s^{-1}} \right) P^2 L_{37} syr^{-1} \tag{2.13}$$

where I_{45} is the effective moment of inertia in units of 10^{45} g cm^2. Physical properties of the wind are highly variable in time and this variability is reflected on $\dot{P}$ and L. It is meaningful to elaborate the behavior of the function $\dot{P}(L)$ dependent on density and velocity of the stellar wind. In the first condition, wind density ρ_W is variable but the capture velocity υ_0 is constant. This condition applies when $\upsilon_{orb}^2 \gg \upsilon_W^2 + c_s^2$. Here, r_a and l_a are constant with $\dot{M} \propto \rho_W$ and $-\dot{P} \propto L^2$. Contrary to the first, second condition consists of a variable υ_0 with a constant ρ_W. This situation causes $r_a \propto \upsilon_0^{-2}$, $l_a \propto \upsilon_0^{-4}$, $\dot{M} \propto \rho_W^4$ and $-\dot{P} \propto L^2$. Finally, both ρ_W and υ_0 may vary with the condition that $\rho_W \upsilon_0$ =constant. This case brings $r_a \propto \rho_W^2$, $l_a \propto \rho_W^4$, $\dot{M} \propto \rho_W^4$ and $-\dot{P} \propto L^2$ (Ghosh & Lamb, 1979).

Of course, gravitational field is not the only entity that influences infalling material. Since plasma approaching the magnetized neutron star is diamagnetic, it enforces field lines of the neutron star to close on in themselves inside a radius r_m. This creates a magnetopause for this infalling material at the point where magnetic pressure of the compact object is equal to the pressure caused by gravitationally bound plasma. This distance is called the magnetospheric boundary for spherical accretion, r_m^s,

$$r_m^s = \left[\frac{1}{2}\frac{v_{in}(r)}{v_{ff}(r)}\right]^{2/7} \mu^{4/7}(2gM_x)^{-1/7}\dot{M}_x^{-2/7} \tag{2.14}$$

$$\approxeq 5.2 \times 10^8 \mu_{30}^{4/7}\dot{M}_{16}^{-2/7} m_x^{-1/7} cm \tag{2.15}$$

where μ_{30}, m_x and I_{45} are the magnetic dipole moment in units of 10^{30} Gcm^3, the mass in units of solar mass ($m_x = M_x/M\odot$) and the moment of inertia in units of 10^{45} gcm^2 of the netron star, respectively. Lastly, v_{ff} is the free fall velocity and $v_{in} = 0.1v_{ff}$. Here, accretion depends on the accretion radius (Equation (3.1)), the radius of the magnetospheric boundary and the corotation radius (Nagase 1989). When $r_m^s < R_a$ and $r_m^s < r_{co}$, infalling matter passes the accretion radius and comes all the way down to the magnetospheric boundary where the confrontation with magnetosphere causes a shock without collision. Details regarding the shock front and its penetration through Alfvén radius will be explained in detail in the following section about Quasi-Spherical Accretion Theory.

2.5 Quasi-Spherical Accretion

X−Per is a good candidate to test the quasi−spherical accretion theory of Shakura et al. 2011. The calculations carried out in Lutovinov et al. (2012) show that this model is successful in explaining the observed spin−luminosity correlations for X−Per. Before elaborating on the conditions and implications of applying this model on X−Persei, a brief description of the Quasi−Spherical Accretion Theory is called for.

2.5.1 Theory of Quasi-Spherical Accretion on X-Ray Pulsars

This model explains the accretion onto slowly rotating magnetized neutron stars in X−ray binaries. Quasi−spherical accretion can take place in systems where the donor star is of early spectral type (O−B) which did not fill its Roche Lobe and is accreting via its stellar wind instead of Roche lobe overflow (RLO). There is no permanent accretion disk in this picture, although temporary disks of accreted plasma can be formed around the compact companion.

Quasi−spherical accretion is mainly characterized by two different regimes. The classical Bondi−Hoyle−Littleton accretion regime can be observed for X−ray luminosities higher than 4×10^{36} ergs/s whereas the settling regime sets in for lower X−ray luminosities. At even higher accretion rates, hence higher luminosities, accretion tends to be highly unstationary as a result of rapid Compton cooling. In a recent paper published in 2012 by Shakura et al., it is established that subsonic settling regime itself can further be analyzed in two different regimes. It is possible that the same source can switch between different accretion regimes during its lifetime.

In accreting binaries where there is no RLO, the stellar wind of the optical companion is gravitationally captured by the neutron star at the Bondi radius. This results in a bow shock formation in the vicinity of the compact object. As one approaches the characteristic radius of gravitational matter capture R_a, the velocity of the wind approaches to a value of V_w, with matter velocity approaching to orbital velocity of the pulsar. Matter accretion onto the compact object results in changes of spin rate because of the torques applied to the compact object in most of these systems. According to the mass accretion rate and how it is transferred inside the binary, both spin-up and spin-down torques are possible. The net torque is,

$$K = K_{su} + K_{sd} \tag{2.16}$$

The torque applied to a system with stellar wind accretion is proportional to Equation (2.9), which can be modified to include the Bondi radius as,

$$K_{su} = \dot{M}\omega_B R_a^2 \tag{2.17}$$

where $\omega_B = 2\pi/P_B$ is the binary orbital angular frequency. For disk-fed systems, torque values have much more simplified expressions, free of complicated time dependencies. The spin-up torque value for disk accretion is defined by,

$$K_{su} \approx \dot{M}\sqrt{GMR_A} \tag{2.18}$$

The first approximation for the spin down value of disk accretion goes as,

$$K_{sd} \sim -\frac{\mu^2}{R_c^3} \tag{2.19}$$

which is independent of mass accretion rate. For wind accretion, on the other hand, there is no specific relation for spin down torque since it is not possible to write a simplistic equation as seen in the disk accretion model. This complication occurs because, for slowly rotating pulsars, r_c is much larger than r_a where the angular momentum transfer occurs, which renders the use of r_c meaningless.

These calculations are good approximations to the torque values experienced by the system, however they slightly reflect the real initial boundaries HMXBs are subject to. In reality, HMXB orbits are not circular, since supernova explosions that gave birth to neutron stars inside these systems give them a wide variety of eccentricities. Also, stellar winds produced by early type stars are highly vari-

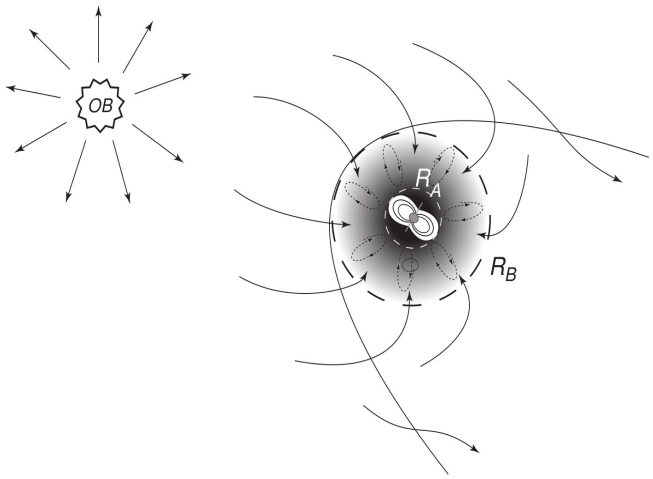

Figure 2.9: Simple schematic of a binary which undergoes quasi-spherical accretion where R_A is the Alfvén radius and R_B is the Bondi matter capture radius (Shakura et al. 2013).

able and inhomogeneous. These conditions generally result in time−dependent spin−up torques $K_{su}(t)$ rather than K_{su}.

2.5.2 Classical Bondi-Hoyle-Littleton Accretion Regime

In Bondi accretion regime, matter heated behind the shock can be rapidly cooled down via Compton scattering. This situation occurs when there is sufficiently high photon density in the region of the shock. Since X−ray luminosity coming from the accretion column, hence the X−ray flux is high, incoming high energy plasma can effectively be cooled down by the rapid interactions with X−ray photons coming from near the neutron star.

In this regime, time scale for cooling down is that of the Compton cooling,

$$t_C = \frac{3}{2\mu_m}\frac{\pi R_a^2 m_e c^2}{\sigma_T L_x} \approx 10.6[s] R_9^2 \dot{M}_{16}^{-1} \approx 1060[s]\dot{M}_{16}^{-1}(\frac{R}{10^{10}cm})^2 \qquad (2.20)$$

where m_e is the electron mass, σ_T is the Thomson cross section, $L_x = 0.1\dot{M}c^2$ is the X-ray luminosity, T is the electron/ion temperature, T_x is the X-ray temperature and μ_m is the molecular weight. Compton cooling time scale is

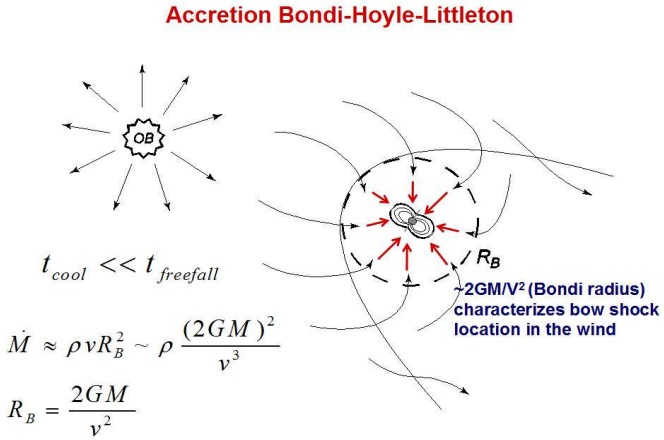

Figure 2.10: Bondi-Hoyle-Littleton accretion regime with relevant cooling time scale and mass accretion rate (Shakura et al. 2014).

smaller than free fall time scale which is defined as,

$$t_{ff} = \frac{R_a^{3/2}}{\sqrt{2GM}} \tag{2.21}$$

Therefore, plasma can be cooled down in a short time and it starts to fall onto neutron star magnetosphere freely, eventually attaining supersonic velocities. Supersonic matter cannot accumulate on the magnetosphere which results in the determination of the mass accretion rate solely by gravitational mass capture rate, $\dot{M} = \rho_W R_B^2 V_W$ suggested by classical Bondi−Hoyle−Littleton accretion formulas.

2.5.3 Settling Accretion Regime

If the system exhibits low to moderate X−ray luminosities, the plasma cannot find time to cool down significantly. As the matter is not cool enough, its radial velocity remains subsonic and plasma tends to pile up on the magnetosphere, forming a hot quasi-spherical shell. Here, accretion onto the neutron star is dependent on the ability of the plasma to enter the magnetosphere. This penetration is incorporated by the instabilities at the bottom of the shell, meaning this plasma, which is in contact with the magnetosphere should cool down in order to continue accreting. In this situation, mass accretion rate is regulated by the density of matter above the magnetosphere as well as the mean velocity of the matter moving towards the base of the shell. The rate of accretion can be small if the cooling of the plasma is ineffective above the magnetosphere. Formation of instabilities, hence the behavior of mass accretion can be described in terms of a critical temperature T_c,

$$RT_{cr} = \frac{1}{2(1+\gamma.m_t^2)} \frac{\cos\chi}{\kappa R_A} \frac{\mu_m GM}{R_A} \tag{2.22}$$

This relation describes the equation of state of the plasma, relating its temperature to the plasma pressure, where the magnetosphere has a local curvature of κ, χ is the angle between the radius vector and the vector that is normal to the given surface element. The factor $(1 + \gamma + m_t^2)$ introduces the turbulent pulsations in the plasma to the total pressure, where m_t is the turbulent Mach number. The boundary between the plasma and the magnetosphere is stable if

the temperature of the environment, T, is higher than T_c but it starts to become unstable below T_c. The boundary can be considered in equilibrium at $T = T_c$.

Besides accommodating the accretion stream, quasi−spherical shell also mediates angular momentum interchange between the accreting plasma and the neutron star. Commonly, angular momentum is removed from the spinning magnetosphere via substantial convective motions in the shell. The removal of angular momentum can also take place without accretion, by the ejection of matter from magnetospheric boundary during the propeller regime. During settling accretion, motion of the fluid elements get quite complicated due to turbulances and instabilities taking place in the shell. As mentioned above, settling accretion can behave differently even under the same external conditions regarding the stellar wind, ie. the density and the velocity of the wind. Although these parameters define the behavior of the regime in most part, characteristic cooling time of the plasma above the magnetosphere also plays an important role in shaping them.

Above the Alfvén surface, two regimes with separate cooling mechanisms can take place during subsonic settling. These are the Compton regime with small time scale, Eqn. (2.20), and the radiative regime with longer time scale, which is described as,

$$t_{cool} = \frac{3kT}{2\mu_m n_e \Lambda} \tag{2.23}$$

where ρ is the plasma density, $\mu_m = 0.6$ is the molecular weight, $n_e = Y_e \rho / m_p$ is the electron number density and for the fully ionized plasma with solar abundance $Y_e \approx 0.8$. Finally, Λ is the cooling function, to which, detailed approximations are shown in the reference (Shakura et al. 2013). For the accretion shell to be formed, cooling time scale must be longer than the time needed for the motion and hence, heating of the plasma. In other words, accretion shell can only be formed if the matter crossing the bow shock region does not cool down too rapidly, which inhibits the free-fall of the matter onto the neutron star. Here, cooling mechanism of interest is the Compton scattering. Compton cooling can only be effective where the temperature of the plasma is smaller than the X-ray temperature. X-ray temperature, temperature of the plasma and Compton cooling time scale are related with each other and the temperature change during

cooling with,

$$\frac{dT}{dt} = -\frac{T - T_x}{t_c} \tag{2.24}$$

where T_x is the X-ray temperature and can be approximated as the photon temperature from the X-ray energy spectrum of a source. Hence, Compton cooling is expected for $T < T_x$. For $T = T_x$, Compton cooling leaves its place to Compton heating, meaning the same process is now causing the incoming particles to gain energy. However, the efficiency of the Compton effects decrease as the distance from the photon source increases. At a larger radii of about 10^{12} cm, time scale for Compton scattering is much longer than the time scale of the gas accretion. Here, photoinoization comes into play as the mechanism of heating. Time scale related to the photoionization heating is,

$$t_{pi} = \frac{(3/2)kT_{max}/\mu_m}{(h\upsilon_{eff} - x_{eff})n_\gamma \sigma_{eff} c} \approx 2 \times 10^4 [s] \dot{M}_{16}^{-1} \tag{2.25}$$

where $\upsilon_{eff} \sim 10$ keV is the characteristic photon energy, ξ is the effective photoionization potential, $\sigma_{eff} \sim 10^{-24}\ cm^2$ is the typical photoionization cross−section and n_γ is the photon number density. There is a specific gravitational mass capture radius for this photoionization-heated zone, R_a^* defined by,

$$R_a^* = \frac{2GM}{c_s^2} = \frac{2GM}{\gamma R T_{max}/\mu_m} \approx 3.5 \times 10^{12} cm \left(\frac{T_{max}}{5 \times 10^5 K}\right)^{-1} \tag{2.26}$$

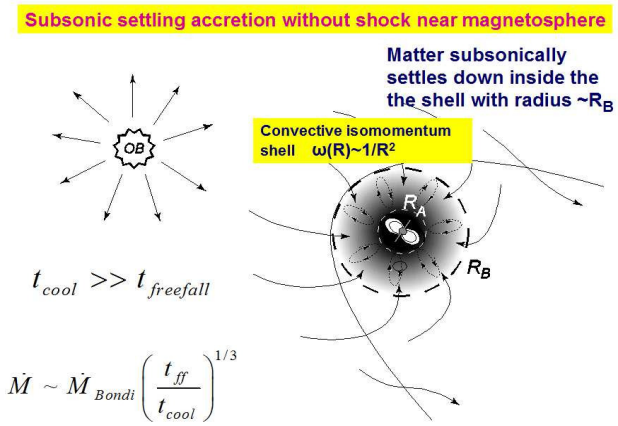

Figure 2.11: Subsonic settling accretion regime with relevant cooling time scale and mass accretion rate (Shakura et al. 2014).

which is larger than the R_a. Here $T_{max} \approx 5 \times 10^5 K$ is the maximum temperature that the gas can be heated via photoionization (Tarter et al. 1969). Corresponding sound speed for this temperature is estimated as 80 km/s.

Quasi-spherical accretion can be described in terms of wind velocities as well. Encapsulating the subject, at small wind velocities around or smaller than 80 km/s (which is the sound speed at maximum temperature for photoionization), accreting plasma will form a bow shock, cool efficiently and fall freely. Cool plasma will approach the gravitating center, meanwhile the photoionization heating will be of importance. This will result in classical Bondi accretion. However, under the condition that maximum temperature of the plasma established from photoionization heating is greater than the adiabatic temperature of the environment, these external conditions may also result in settling accretion. At high wind velocities that are greater than 100 km/s with a post-shock temperature higher than T_{max}, photoionization is unimportant and settling accretion regime will occur with the conditions described earlier. A comparison of radiation cooling and accretion time scales gives the critical accretion rate as a function of the wind velocity below which the settling accretion regime is possible as,

$$\dot{M}_{16}^{cr} \lesssim 0.12 v_7^{3.2} \tag{2.27}$$

On the contrast, accretion rate of $\dot{M} = 4 \times 10^{16}$ gives a boundary value above which a free fall gap appears above the Alfvén surface and no accretion is possible (Shakura et al. 2011).

2.5.3.1 Settling Accretion and the Power Spectrum

Fourier transform obtained from the time series of X−ray pulsars mainly reveal the radiation coming from the accretion column. Besides the accretion column, hot quasi-spherical shell generates its own thermal emission as well and is successful in radiating it since it is optically thin. However, even at full efficiency, which means the release of all gravitational energy at the shell, this radiation cannot be dominant in the power spectrum because it is only a small part of the whole since the radiation is scaled as the diameter of the emitting region. Here,

$$\frac{L_{x(shell)}}{L_{x(acc)}} \sim \frac{R_{shell}}{R_{acc}} \sim \frac{R_{mag}}{R_{NS}} \sim 0.01 \tag{2.28}$$

Furthermore, X−ray spectrum of accretion column is hardly affected by the scattering in the hot shell. Although the shell is not very effective on the power spectrum, it can trigger features in free-fall time scale in the variability of the spectrum via large scale convective motions. QPOs formed by this process are expected to have frequency values of the order of mHz. Additionally, 1000 second features are expected to be observed because of the strong effect of dynamical instability (possibly,of collapse) of the shell caused by increased Compton cooling and increased mass accretion rate (Shakura et al. 2013).

Formation of temporary, altough long term, accretion disks around the compact object are not unusual for Be type HMXBs when the angular momentum of the incoming material is sufficient enough. The occurrence of quasi-periodic oscillations in these systems are taken to be the indication of a disk formation. According the 2−D simulations carried out by Blondin et al. 1990, slower stellar wind velocity of the optical companion implies larger accretion radius which enables disk formation. This disk is similar to a standard viscous accretion disk and is formed inside the bow shock. It is assumed that temporary accretion disks shape around the neutron star during outbursts in HMXB and they deform when the system luminosity reduces to normal values (Wilson et al. 2008).

2.5.3.2 Period Variations During Settling Accretion

Settling accretion and consequent shell formation around the magnetosphere can result in both spin−up and spin−down of the neutron star which ultimately depends on the sign of the angular velocity difference between the accreting matter and the magnetospheric boundary. During settling phase, accretion rate is dependent on the density of the shell close to the Alfvén surface as well as its ability to penetrate it. The rotation of this shell is effected by the viscosity turbulances, which are anisotropic because of the convective motions. The angular velocity of the shell is dependent on the radius as,

$$\omega(R) \sim R^{-n} \tag{2.29}$$

By making use of the quasi-Keplerian and iso-angular momentum approximations with $n = 3/2$ and $n = 2$ respectively and introducing the Bondi radius to the relation, one gets the angular velocity of the matter at the bottom of the shell as,

$$\omega_m = \tilde{\omega}\omega_B \left(\frac{R_B}{R_A}\right)^n \tag{2.30}$$

Comparing the spin angular velocity of the neutron star, $\omega^* = 2\pi/P^*$ (where P is the spin period) with ω_m provides information about the direction of the transfer of angular momentum. If $\omega^* > \omega_m$, angular momentum is transferred from the magnetosphere to the shell. Otherwise, if $\omega^* < \omega_m$, than the angular momentum is transferred from the shell to the magnetosphere of the star. This transfer takes place due to the coupling between the magnetosphere and the shell.

Coupling can be strong or moderate, depending on the strenghts of the magnetic field components. For a strong coupling to take place, toroidal magnetic field component B_t should grow large enough to approximate the strength of the poloidal field component, B_p. This behavior can be observed for fast spinning magnetospheres with ω^* comparable to the Keplerian angular frequency, ω_K . $\omega^* > \omega_K$ means that the system is in the propeller state where there is no accretion. In the moderate coupling state, instabilities at the magnetosphere enables the plasma to penetrate it in a shorter time than required for B_t to reach the value of B_p. Hence, during moderate coupling toroidal field component is smaller than that of the poloidal field. The strong coupling regime constitutes an extreme case for the state of the shell and the magnetosphere. Commonly, the communication of angular momentum with these two entities are easily carried out by various plasma instabilities within a time scale shorter than needed for a strong coupling. Therefore, the case of moderate coupling is more general and instructive and hence, will be discussed as a means of understanding the nature of the momentum transfer during quasi-spherical accretion.

Plasma at the bottom of the shell, side by side with the magnetosphere, is too hot to be able to penetrate inside and is quite stable if it does not cool down. Instabilities such as the Rayleigh-Taylor instability start to take place when the plasma cools down via Compton scattering because of its interactions with the

X-ray photons coming from the poles of the neutron star.

After taking into account the Rayleigh-Taylor instability which has the highest probability of occurance and toroidal magnetic field increase with time, a spin-down formula is reached for the moderate coupling, following the calculations in Shakura et al. 2013. Without going into the calculation details, relation for the change of neutron star angular velocity is given as,

$$I\dot{\omega}^* = Z\dot{M}R_A^2(\omega_m - \omega^*) + z\dot{M}R_A^2\omega^* \tag{2.31}$$

Here, I is the moment of inertia of the neutron star, z is a numerical factor that accounts for the geometry and angular momentum of the infalling plasma. z takes values from 0 (matter falls along the spin axis) to 1 (matter falls from the equatorial equator) and in a special case where matter falls over the entire magnetosphere, z has the value 2/3. Z is a dimensionless coefficient (equation 26 in Shakura et al. 2013). As can be seen, removal of the angular momentum from the neutron star can take place if $Z > z$, which would result in a spin−down. Otherwise, with $Z < z$, the neutron star can spin−up. In the case that a hot shell is not formed, $Z = z$ and the sign difference between angular velocities of the shell and the magnetosphere becomes irrelevant to the discussion. When the hot shell forms, Eqn. (2.29) is valid and can be substituted into Eqn. (2.30) as ω_m, which gives,

$$I\dot{\omega}^* = Z\dot{M}\tilde{\omega}\omega_B R_B^2 \left(\frac{R_A}{R_B}\right)^{2-n} - Z(1 - z/Z)\dot{M}R_A^2\omega^* \tag{2.32}$$

This relation describes the angular momentum transfer and the dependence of angular velocities of the shell and the magnetosphere in the moderate coupling regime during the settling accretion. Evidently, spin−up/spin−down behavior of the neutron star is related to the angular velocities and the change in $\dot{M}$. Although mass accretion rate is directly dependent on the density of the matter in the shell at the magnetospheric boundary, mass capture rate variations caused by the changes in the stellar wind are transmitted to this region as well. The most important parameter affecting the density at this region is the variation in the stellar wind velocity. Again, avoiding to go into lenghty calculation details, Eqn. (2.31) can be written in terms of $\dot{M}$, with the help of the dimensionless parameter $y \equiv \frac{\dot{M}}{\dot{M}_{cr}}$, where $\dot{M}_{cr}$ is the value of $\dot{M}$ at which $\dot{\omega}^*$ reaches its absolute

minimum value. The equation is derived as,

$$I\dot{\omega}^* = A\dot{M}_{cr}^{(3+2n)/11} y^{(3+2n)/11} \left(1 - \left(\frac{y_0}{y}\right)^{\frac{2n}{11}}\right) \tag{2.33}$$

where $y_0 = \left(\frac{3+2n}{3}\right)^{\frac{11}{2n}}$ and A is a coefficient that is independent of the accretion rate. Variation of this relation with respect to y gives,

$$I(\delta\dot{\omega}^*) = I\frac{\delta\dot{\omega}^*}{\delta y}(\delta y) = \frac{3+2n}{11} A\dot{M}_{cr}^{\frac{3+2n}{11}} y^{-\frac{8-2n}{11}} \left(1 - \frac{1}{y^{\frac{2n-1}{11}}}\right)(\delta y) \tag{2.34}$$

From this relation, the expected behavior of y with respect to $\dot{\omega}^*$ is obtained. Fig. (2.12) shows that at specific critical mass accretion rates $\dot{M}_{cr}$, these systems experience spin reversals.

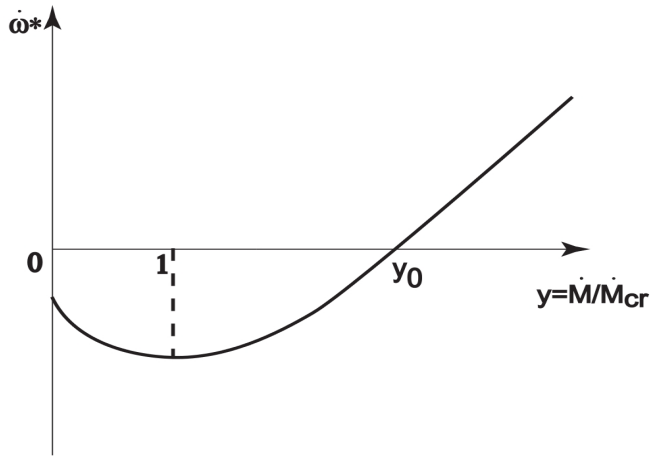

Figure 2.12: Plot of the frequency derivative with respect to the parameter y (Shakura et al. 2013). Flux of the source is related to the y parameter with a multiplicative constant.

CHAPTER 3

APERIODIC VARIABILITY IN X-RAY BINARIES

Aperiodic variability is constituted of features in the time series of X-ray sources that do not manifest themselves regularly. Periodic events that are known to be repeated in time by the source due to a certain physical process, such as pulsations, eclipses and outbursts are not considered in this group. Irregular phenomena such as sporadic flaring, flickering and fluctuations, on the other hand, are variabilities that are not periodic. These variations in LMXB light curves are most likely connected to erratic accretion patterns of these systems. For HMXBs, effects of the magnetic field of the compact object adds to the irregular inner accretion flow and results in an even more complicated picture (Reig 2011).

A convenient way to study these phenomena is by producing the Fourier power spectra of count rate time series. All power spectra are composed of several variability components and a continuum, both of which can show various structures characteristic of sources. Unlike the sharp appearance of periodic pulsations, aperiodic variability components extend to several frequency bins on power spectra. Broader features are designated as noise while narrow structures are termed quasi−periodic oscillations.

Origin of this variability is thought to be the alternations in the flow of matter onto the neutron star. Range of quasi−periodicity frequencies observed for low mass and high mass systems span a few orders of magnitude from millihertz in accretion powered pulsars and HMXBs to kilohertz in LMXBs. Kilohertz variations observed from low mass binaries can only be attributed to the motion

Table3.1: List of accretion powered QPO sources with high magnetic fields (Devasia et al. 2011).

Source	Type	ν_s (mHz)	ν_{QPO} (mHz)	ν_{QPO}/ν_s
Transient pulsars				
KS 1947+300	HMXB/Be	53	20	0.38
SAX J2103.5+4545	HMXB/?	2.79	44	15.77
A0535+26	HMXB/Be	9.7	50	5.15
V0332+53	HMXB/Be	229	51	0.223
4U 0115+63	HMXB/Be	277	62	0.224
1A 1118–61	HMXB/Be	2.5	92	36.8
XTE J1858+034	HMXB/Be	4.53	110	24.3
4U 1901+03	HMXB/?	361.9	130	0.359
EXO 2030+375	HMXB/Be	24	200	8.33
SWIFT J1626.6-5156	HMXB/Be	65	1000	15.38
XTE J0111.2-7317	HMXB/B0.5-B1Ve	32	1270	39.68
GRO J1744-28	LMXB	2100	20000	9.52
Persistent pulsars				
SMC X-1	HMXB/B0	1410	10	0.0071
Her X-1	LMXB	806	13	0.016
LMC X-4	HMXB/O-type	74	0.65-20	0.0087-0.27
Cen X-3	HMXB/O-type	207	35	0.17
4U 1626-67	LMXB	130	48	0.37
X Per	HMXB/Be	1.2	54	45
4U 1907+09	HMXB/OB	2.27	69	30.4

of the matter very close to the neutron stars' intense gravitational field. These frequencies coincide to dynamical time scales of the order of 0.1 ms at ∼15 km and ∼2 ms at 10^2 km from a $1.4M_\odot$ and $3R_{sch}$ neutron star which has a radius about 10^2 km from a 10 solar mass black hole (Van der Klis 2004). Quasi periodic oscillations, forming within few Schwarzschild radii, provide a unique opportunity to probe the behavior of the dense matter under strong gravity.

Although general theory of relativity has been tested under weak gravitational fields, its confirmation by direct observations of the motions of particles in strong gravitational fields remains undone. Surroundings of black holes and neutron stars are perfect examples for these regions of space where gravitational binding energies are of the order of rest masses. Testing the predictions of general relativity at these regions such as the existence of innermost stable circular orbit (ISCO), dragging of inertial frames and general relativistic precession rates via observational data reveals further information about the nature of the universe. Furthermore, analysing the dense matter interactions through pressure-density-temperature relations of bulk matter, reveals some important relations

for microphysics (LOFT Yellow Book, ESA 2013). It is possible to probe the fundamental properties of matter by constraining the mass-radius relation for neutron stars using the knowledge of the behavior of plasma surrounding them, which is exposed to extreme conditions.

3.1 Aperiodic Variability in HMXBs

Aperiodicity in HMXBs are in the milliHz range and cover the frequency interval few orders of magnitude lower than LMXB, in between 1−400 mHz. In James et al. 2011, it is reported that there are 13 HMXBs with QPO detection in their spectra so far. 9 of these systems are BeXRBs (Table 3.1).

In contrast to LMXBs prominent and peaked QPOs, most of the HMXB quasi-periodicities have very low quality factors which put them in the class of peaked noise rather than genuine QPOs (when Q<2). This inconsistency is not daunting however, since on the totality of power spectra these noise features still embody a considerable amount of power in a narrow frequency range hence are being called quasi−periodic oscillations (Reig et al. 2013).

As mentioned before, formation of QPOs are attributed to the inhomogeneous flow of the accreting matter. Resulting via the same process, difference between frequencies of LMXB and HMXB QPOs can be explained by considering the structure of the accretion disk. Longer time scales for the Keplerian motion of plasma around the neutron star in an HMXB implies that inner radius of the accretion disk is larger than the radius of the magnetosphere. QPOs in the range 10−400 mHz can be expected from a disk radius of $10^8 - 10^9$ cm. QPOs observed in the range 0.1−60 Hz disclose the information from strong gravity fields, ie. occurance of Lense−Thirring Precession and probes relativistic motions of the particles (LOFT Yellow Book, ESA 2013). Hence, examination of not only LMXB QPOs but also HMXB QPOs are of importance regarding key points discussed in the last section since this frequency range is satisfied by aperiodic variability seen in some high−mass systems as well. Before discussing the applicability of the current QPO models to HMXB QPOs in specific, it is

timely to introduce the three models most relevant to this work.

3.1.1 Keplerian Frequency Model (KFM)

In the Keplerian Frequency Model proposed by Van der Klis et al. in 1987, quasi−periodic features in the X−ray emission is caused by the accumulations of matter that remain together during their motions around the neutron star. These pile ups modify the X−ray flux by obscuring the emission coming from behind them close to the magnetospheric boundary. Their movements in the disk, therefore the oscillations they produce are seen with the Keplerian frequency at that radius (Camero−Arranz et al. 2012). For spherical accretion, a $1M_{\odot}$ neutron star with a radius of 10^6 and with $r_m \sim 0.5r_a$, the QPO frequency is the Keplerian frequency at r_m,

$$\upsilon_k(r_m) = 1.05\mu_{30}^{-6/7} L_{37}^{3/7} Hz \tag{3.1}$$

with μ being the magnetic dipole moment of the neutron star in units of 10^{30} G.cm^3 and L_{37} is the accretion luminosity in 10^{37} ergs/s (Angelini et al. 1989).

A key point in this model is the comparison of spin frequency to the Keplerian frequency of the inner accretion disk. If the spin of the neutron star is higher than the azimuthal motion of the disk, mass accretion at the magnetospheric boundary is no longer possible because of the centrifugal inhibition of infalling matter. At this stage, while the propeller effect is at work, Keplerian frequency model is not applicable (Dugair et al. 2013).

3.1.2 Beat Frequency Model (BFM)

This model, proposed by Alpar and Shaham in 1985, again considers the plasma moving at the inner radius of the accretion disk. In contrary to KFM, BFM assumes the emission of matter blobs around the magnetosphere (Belloni & Hassinger, 1990). Structures contained in the accretion disk near this radius move with local Keplerian frequencies. These blobs of matter gradually shift toward the neutron star via disk's radial motion. When close enough, at the

Alfvén radius, they are threaded by the magnetic field of the neutron star resulting in their vertical motion following the field lines and removal in time by falling onto the star. This region, where plasma is strongly controlled by the stellar magnetic field, starts at the radius where the ram/magnetic pressure is equal to the pressure of the Keplerian disk, r_a. Defining r_a in terns of convenient units one has,

$$r_a \sim R_0 \sim 10^6 B_8^{4/7} R_6^{12/6} \dot{M}_{17}^{-2/7} \left(\frac{M}{M\odot}\right)^{-1/7} cm \tag{3.2}$$

where B_8 denotes the surface magnetic dipolar field in units of 10^8 G, R_s is the stellar radius in units of 10^6 cm, M and $M\odot$ are stellar and solar masses, respectively, and $M\odot^{17}$ is the total mass accretion rate in units of 10^{17} g/sec. In other words, for surface fields greater than 10^6 Gauss, R_0 forms the boundary between magnetic field and gravity field dominated regimes. The Keplerian angular velocity at R_0 equals to,

$$\omega_0 = \left(\frac{GM}{R_0^3}\right)^{1/2} \sim 10^4 B_8^{-6/7} R_6^{-18/7} dot{M_{17}}^{3/7} \left(\frac{M}{M\odot}\right)^{5/7} rad/sec \tag{3.3}$$

At first look, it seems the mass accretion rate in this relation has the potential of introducing variability to the outcome. When this is the case, Keplerian angular velocity is dependent on mass accretion rate and ultimately to the count rate. Apparent weakness of this dependence when compared to the observational data has led the authors to identify the QPO frequency ($\upsilon_{QPO} = f/2\pi$) with the beat frequency,

$$\omega_B = \omega_0 - \omega_S \equiv A\dot{M}^{3/7} - \omega_S \tag{3.4}$$

where ω_s is the spin velocity of the neutron star and A is a constant. With the assumption that the stellar rotation axis is perpendicular to the disk, this relation describes the removal of plasma blobs with the beat frequency between the Keplerian disk and the rotation frequency of the stellar magnetic field, which is equal to the neutron star spin frequency since the magnetic field is anchored to the compact star (Camero−Arranz et al. 2012). In this model, increase of the accretion rate results in an increase in local Keplerian frequencies and ultimately the beat frequency of the QPO (Stella et al. 1999).

A couple of scenarios have been proposed to explain the physical mechanism producing the beat frequency as an outcome. It is straightforward that any

mechanism causing QPOs at the beat frequency should take place at R_0 via the modulation of the accretion flow where the accretion is not hydrodynamical. This implies that the plasma surrounding the region of interest is locally magnetized in itself, at least until crossing R_0. A primary assumption is the existence of a "magnetic gate". Here, incoming plasma is previously magnetized, by the stellar magnetic field at the r_{co}, for example. This magnetization than leads to the intermittent breach of R_0 by the infalling plasma. At R_0, stellar field and plasma magnetizations are opposite, causing occasional field reconnections that will also adjust the matter flow at the beat frequency. Besides being modulated by the magnetic field interactions, matter may be coming in as real blobs of plasma, a suggestion that will also satisfy this model. Another suggestion that draws attention to the real geometrical structure of the magnetic axes of the neutron stars. If the magnetic axis is at an angle to the rotation axis, there is a possibility that the magnetospheric boundary surrounding the neutron star is not circular. Instead, this can be any closed curve with a mirror symmetry through its center. When this kind of a geometry is observed, it is possible that a modulation in the accretion flow is seen, without the need of the magnetized material or the exclusion of an hydrodynamic flow (Shaham 1987).

As with KFM, BFM also assumes a centrifugal inhibition threshold, a property that cannot be observed at some sources with assumed BFM QPOs (Finger 1998).

Magnetospheric Beat Frequency Model can be related to the fastness parameter providing a further insight to the interactions of the disk and the magnetosphere as well as the accretion torques. Equation disclosing the relationship between the fastness parameter, neutron star spin and QPO frequencies is,

$$\omega_s = \frac{\upsilon_s}{\upsilon_s + \upsilon_{QPO}} \tag{3.5}$$

where $\omega_s = \upsilon_s/\upsilon_k$ is the fastness parameter, υ_s and υ_{QPO} are the neutron star spin and QPO frequencies respectively (Ghosh 2007).

3.1.3 Magnetic Disk Precession Model (MDPM)

Another model that can explain the low frequency QPOs in accretion−powered X−ray binaries is the magnetic disk precession model proposed by Shirakawa and Lai in 2002. Authors explain quasi−periodicities in terms of warping and precession motions of the disk at the magnetospheric boundary due to magnetic field effects. These effects are induced by the interactions of the stellar wind and the electric currents circulating in the disk (Dugair et al. 2013).

3.1.4 Applicability of the Models to Data from Accretion Powered X-Ray Sources

KFM and BFM can explain QPO frequency ranges of some HMXB sources. However, since their predictive power is not valid for all sources, it can fairly be assumed that the origin of the mHz QPOs still elude current models. MDPM, on the other hand, brings some new insights that account for unexplained QPOs, yet it's applicability on all sources is not clear as of now (Reig et al. 2013 and references therein).

It is informative to summarize the discovery and the interpretation of QPOs in HMXBs that have been published so far, in order to shape the perspective with which findings from X−Per will be examined. Transient high−mass X−ray binaries with QPO detections in their power spectra are as follows; EXO 2030+375 (Angelini et al. 1989), A 0535+262 (Finger et al. 1996), 4U 0115+63 (Soong & Swank 1989) and V 0332+53 (Takeshima et al. 1994), 1A 1118–61 (Devasia et al. 2011), SAX J2103.5+4545 (Inam et al. 2004), XTE J1858+034 (Paul & Rao, 1998), 4U 1901+03 (James et al. 2010), SWIFT J1626.6–5156 8 (Reig et al. 2008), XTE J0111.2−7317 (Kaur et al. 2007). There are some persistent high−mass systems with quasi−periodic fluctuations as well, such as Cen X−3 (Takeshima et al. 1991), SMC X−1 (Angelini et al. 1991), X Persei (Takeshima 1997) and 4U 1907+09 (in't Zand et al. 1998). It is reported that both KFM and BFM are suitable for explaining QPOs seen in EXO 2030+375, A 0535+262, 1A 1118–61, XTE J0111.2−7317, 4U 1907+09, however for 4U

0115+63, V 0332+52, Cen X−3, 4U 1626−67, SMC X−1 , Her X–1, LMC X−4, V 0332+52 and KS 1947+300 QPO frequency is lower than the spin frequency of the neutron star meaning KFM is not applicable to these sources. For XTE J1858+034 and SAX J2103.5+4545, KFM seems to be a good approximation. BFM works for the QPOs seen in the spectra of 4U 1901+03. In the case of V 0332+52, BFM is in disagreement with observational data since calculations of magnetospheric boundary gives different results for evaluation from QPO properties and from observed luminosity of the source.

As can be seen, BFM seems to agree with most of the observations. Nevertheless, the occasional lack of a positive correlation between QPO line center and X−ray luminosity casts doubt on this model since this is a prediction that BFM makes (Paul & Rao, 1998). For sources neither KFM or BFM can be applied, MDPM is proposed as the new alternative. However, detailed work on the compatibility of this model with real observations remains to be done.

3.2 The Search for Aperiodic Variability in Time Series and Quasi-Periodic Oscillations

A common practice to study the aperiodic variability in a time series data is to make use of Fourier techniques. Through both engineering and sciences, Fourier transform methods have an enormous and irreplaceable effect on our current level of technology and knowledge.

The work of an astronomer in terms of data analysis is not very distinct from that of an electrical engineer working on signal processing. What seems to be irrelevant pursuits are mainly applications of same procedures on different signals of interest. This is why Fourier techniques have become vital in the investigation of astrophysical data as well, which calls for an overall description of the theory of Fourier transform and related signal analysis methods here.

In the scope of X−ray astronomy, timing studies of the neutron stars consist of detecting signals originating from the source against a noise background. Search for QPOs are carried on by transforming the time series or count rates/sec X−ray

photon data at hand, which is in time domain, to frequency domain with the help of Fourier transformation techniques. X−ray observations of eligible sources are uniformly separated binned timing data. Spaces without any information in the data are far away from each other, if they exist, meaning most of the time bins contain data and are not empty. These properties of X−ray timing data, data such as photon counts obtained by an X−ray proportional counter, make it quite suitable for analysis with Fast Fourier Transform (FFT) algorithms.

3.2.1 The Fourier Transform

Fourier transform, developed by Joseph Fourier, is a mathematical procedure that enables the transformation of a signal between time and frequency domains. This enables the approximation of any curve by appropriate series expansions. When continuous and periodic signals are considered, this transformation can be quite straightforward requiring solely the determination of some discrete set of complex amplitudes referred to as Fourier series coefficients. Furthermore, any periodic curve will need less number of elements to be completely described by Fourier series than by power series, hence it is considered that the best representations of periodic signals are obtained via the application of Fourier methods. A signal $x(t)$ can be decomposed to a combination of sine waves by a Fourier transform. When the signal is described as,

$$a\cos(\omega t - \Phi) = A\cos\omega t + B\sin\omega t \tag{3.6}$$

best fit values for a and Φ or A and B represents $x(t)$ in terms of sines and cosines. After a sufficient number of iterations in frequency, the signal can be reconstructed as,

$$x(t) = \frac{1}{N}\sum_j a_j \cos\left(w_j t - \Phi_j\right) = \frac{1}{N}\sum_j (A_j \cos w_j t + B_j \sin w_j t) \tag{3.7}$$

with Fourier coefficients,

$$A_j = \sum_k x_k \cos w_j t_k \tag{3.8}$$

$$B_j = \sum_k x_k \sin w_j t_k \tag{3.9}$$

Fourier coefficients represent the correlation of x_k with a sine or cosine wave of frequency w_j. Simply put, if there is 100 % correlation, A_j and B_j are at their maximum values giving the maximum contribution to the sum in Eqn. (3.7). Depending on the problem at hand, complex representation of the above coefficients proves useful. Complex Fourier amplitudes are defined as,

$$a_j = \sum_k x_k e^{iw_j t_k} \tag{3.10}$$

$$x_k = \frac{1}{N} \sum_j a_j e^{iw_j t_k} \tag{3.11}$$

and a_j are denoted as the Fourier transform of the x_k. The transform is reversible and x_k are referred to as the inverse Fourier transform of a_j.

Timing data is best explained as sequences of bins with each having a number of detected photons x_k. A signal with N number of x_k can be deconstructed to N sine waves with Fourier transform $a_j(j = N/2, ..., N/2)$. Below is the related pair of transformation relations,

$$a_j = \sum_{k=0}^{N-1} x_k e^{2\pi ijk/N} \tag{3.12}$$

$$x_k = \frac{1}{N} \sum_{j=N/2}^{N/2-1} a_j e^{-2\pi ijk/N} \tag{3.13}$$

where $j = -\frac{N}{2}, ..., \frac{N}{2} - 1$ and $k = 0, 1, ..., N - 1$. These equations apply to an equally spaced time series of length T, so that x_k corresponds to a time interval of $t_k = kT/N$ with a time step of $\delta t = T/N$. Frequency series are thus represented by,

$$w_j = 2\pi \upsilon_j = 2\pi j/T \tag{3.14}$$

with a frequency step $\delta f = 1/T$, when transformation from time domain to frequency domain is performed. After these transformations, one obtains the entire explanation of the discrete signal via sine and cosine waves. Highest frequency value needed for this complete description is called the Nyquist frequency which is the half of the sampling frequency N/T, denoted as,

$$\upsilon_{N/2} = \frac{1}{2}\frac{N}{T} \tag{3.15}$$

When dealing with observational information, theoretical approximations to trends in the data are generally carried out with the help of continuous Fourier transform. This is why it is important to extend this discussion to continuous transforms as well, which only had been on discrete transforms so far.

A continuous Fourier transform constructs an infinitely extended continuous function $x(t)$ $(-\infty < t < \infty)$ from an infinite number of sine waves,

$$a(\upsilon) = \int_{-\infty}^{\infty} x(t) e^{2\pi\upsilon it} dt \tag{3.16}$$

$$x(t) = \int_{-\infty}^{\infty} a(\upsilon) e^{-2\pi\upsilon it} d\upsilon \tag{3.17}$$

where $-\infty < \upsilon, t < \infty$. The relationship between discrete and continuous transforms can be explained by making use of the convolution theorem. Given two Fourier transforms $a(\upsilon)$ and $b(\upsilon)$ of $x(t)$ and $y(t)$, convolution is defined as,

$$a(\upsilon) * b(\upsilon) \equiv \int_{-\infty}^{\infty} a(\upsilon^{'}) b(\upsilon - \upsilon^{'}) d\upsilon^{'} \tag{3.18}$$

By convolving a continuous Fourier transform of the infinitely extended continuous function $x(t)$ with two specific functions, $x(t)$ can be discretely sampled and thus, a desired portion of the continuous function can be obtained as a discrete function. This double multiplication consists of a window function for which,

$$w(t) = 1 \qquad\qquad 0 \leq t < T \tag{3.19}$$

and otherwise,

$$w(t) = 0. \tag{3.20}$$

It also consists of a sampling function,

$$i(t) = \sum_{k=-\infty}^{\infty} \delta \left(t - \frac{kT}{N} \right). \tag{3.21}$$

Here, the purpose of window function is to select a certain part of the time series while the sampling function constructs a discrete structure out of a continuous transform by making use of the Dirac-Delta function (Van der Klis 1988).

3.2.2 The Power Spectrum

By making use of Bessel's inequality on a Fourier series expansion, one can evaluate the Parseval's Theorem as,

$$\sum_{k=0}^{N-1} |x_k|^2 = \frac{1}{N} \sum_{j=-N/2}^{N/2-1} |a_j|^2 \tag{3.22}$$

where $j \neq 0$. Applying the normalization defined in Leahy et al. 1983, power spectrum can be defined as,

$$P_j = \frac{2}{N_{ph}} |a_j|^2 \tag{3.23}$$

where $j = 0, ..., N/2$ (Van der Klis 1988).

3.3 Statistical Approaches Related to Power Spectra

3.3.1 F-test

Significances of QPOs are calculated using F-test statistics. F−test is one of the Analysis of Variance (ANOVA) statistical methods. It investigates the variation between and within groups. Assumptions for the variance analysis is compatible with data distributions in lightcurves and power spectra.

In this approach, variables should be normally distributed and independent from each other as well as their variances should be homogeneous. A standard lightcurve consists of data with Poisson distribution. This is expected since each photon falling onto the detector is independent of other photons so the events are not dependent on each other in a fixed interval of time and in a defined amount of space. They are also spread widely in time so as to be described as "rare". These discrete random events are the variables in a lightcurve with a probability mass function (PMF) given as,

$$f_P(k, \lambda) = \frac{\lambda^k \epsilon^{-k}}{k!} \tag{3.24}$$

λ corresponds to the expected value and also to the variance in this case. A power spectrum derived from a Poisson distributed lightcurve is normally distributed

for large numbers of λ as predicted by CLT [1]. Normally distributed data has a PMF,

$$f_G(x) = \frac{1}{\sqrt{2\pi\sigma^2}} e^{\frac{-(x-a)^2}{2\sigma^2}} \tag{3.25}$$

with σ^2 variance and a mean of a. Independence means that there is no correlation between variables, both among themselves and their errors (Monday, Klein and Lee, 2005).

F-test which investigates the difference between variances is suitable for the analysis of power spectra since it enables the measurement of the amount of variance of a signal feature in the continuum as well as its compatibility to the given model, hence probing multiple groups of variables. A basic description of F-test is the ratio of the variance found between groups to the expected variance. The denominator can also represent variance within groups which is unsystematic and solely due to chance. The F value drawn from this ratio is then transformed to a probability. The value of this probability determines how likely it is for the event of interest to occur by chance. If this value is low enough, then there is a solid probability that the event is not observed by chance and is fit to the model. In this case, the null hypothesis which states that there is no relationship within two groups of variables and the phenomena that they represent, thus are in a default or general position, gets rejected. Rejection of the null hypothesis means one can further investigate the relationship between two events with the assurance of a solid ground in claiming one. [2].

3.3.2 RMS Amplitudes and Quality Factors

Besides the significance, a comprehensive QPO investigation should account for two other important characteristics. These are the root mean square (RMS) amplitude and quality factor (Q) of the signal.

RMS amplitudes of quasi-periodicities describe the power of these QPO signals against the continuum and noise features. It is the variation of signal in terms

[1] Central Limit Theorem (CLT) states that when an independent selection is made from a large number of random variables in a certain distribution, mean of the newly formed variable group will be normally distributed, even if the initial distribution is not.

[2] https://www.coursera.org/course/stats1

of its magnitude. RMS amplitude as a percentage is given as,

$$RMS = 100\sqrt{\frac{I}{mean}} \tag{3.26}$$

Here, I represents the integral of the model used to fit the signal (determining the area beneath it) and mean is the mean count rate of the source. The result of this integral is calculated as, $I = \frac{\pi g f}{2}$ for Lorentzian fits and $I = \sqrt{2\pi g f}$ for Gaussian fits, g = line normalization, f = line width. Mean value for each QPO are estimated from the lightcurve segments during which these QPOs are observed. Start and stop times are derived from the power spectra with detections and later used to segment the whole lightcurve to find out the exact intervals where quasi-periodic fluctuations take place[3].

Quality factor, also known as Q value, is simply the ratio of the height of a certain signal against its width. It is used as a measure to understand how broad a feature is. It also describes the amount of damping for an oscillator. A high value of Q means that the energy loss is small compared to the stored energy in the oscillator and it takes a longer time for the oscillations to die out. For a signal, larger Q values indicate that the endurance of the signal is higher hence it can persist in the medium for a comparably long time. By comparing Q values of different signals, it is possible to distinguish genuine QPOs from broader noise features. There exists a general consensus regarding the classification of signals considering their Q values. A certain structure in power spectrum can be conceived as a quasi-periodic oscillation when its Q value is greater than 2, while a Q value lower than 2 implies that this feature is most likely a broad band noise. Quality factors are calculated simply as,

$$q = \frac{linecenter}{linewidth}. \tag{3.27}$$

3.4 X-Persei

X-Persei is a Be type X-ray binary in the Perseus Constellation. It consists of the persistent, low luminosity, long periodic accreting pulsar 4U 0352+309 with an X−ray luminosity of $L_x = 10^{35}$ ergs/s and the B0 Ve type optical companion

[3] http://heasarc.nasa.gov/docs/xte/recipes/

HD 24534. Distance of the source has a rather rough estimation ranging from 700 to 1300 parsecs, with an average of 950 $\pm$ 200 pc proposed by Telting et al. 1998 (Doroshenko et al. 2012, Lutovinov et al. 2012). The system has a pulse period of 837 seconds and an orbital period of 250 days. It was first detected by Copernicus Observatory during a high intensity state (White at al. 1976). The compact object has been identified as a neutron star due to the system's hard X-ray spectrum and the variation in pulse period measured as $\frac{\dot{P}}{P} \sim 10^{-4}\ 1/yr$. The system has a wide and almost circular orbit with an eccentricty of e$\sim$0.11 (Doroshenko et al. 2013 and references therein). The binary has a projected equatorial velocity $v = \sin i$ of 200 km/s. This indicates that HD 24534 is seen from a low or intermediate inclination angle with an orbital inclination of $\sim 23 - 30$ degrees (Clark et al. 2001).

X-Per is distinguished from other sources in its' class by its low eccentricity which results in lack of Type 1 outburst that are normally observed in BeXRBs. This also results in the persistent low luminosity X$-$ray emission from the system with little changes in the luminosity even during Type 2 like outbursts, if any. This X-ray source has an exceptionally low luminosity generally ranging from 10^{34} to $2 - 4 \times 10^{35}$ ergs/s. During its brightest periods, strong H_α and other Balmer lines are seen in the spectra, which qualifies this source as Be type. During the low luminosity periods, these lines dissapear and the optical companion resembles a normal early type star. This variability in the spectra is related to the disappearance and reappearance of the disk around the optical companion (Delgado-Marti et al. 2000).

X-Per is highly variable in optical and infrared emission as it is common with all BeXRBs. The source is known to exhibit large fluctuations in its optical and infrared brightness as well as in its Balmer emission lines. These changes are thought to be related to the Be star companion's disk geometry and density. Despite this variability in longer wavelengths, X-ray luminosity remains relatively constant. This is thought to be due to the truncation of the circumstellar disk as a result of the torques applied by the neutron star. The wide gap produced by truncation restricts the accretion flow at all times, causing low X-ray luminosities and independent variations of the optical brightness. Since Clark et al.

2001 reported the entire disappearance of the disk between May 1988 – June 1989, reformation of the disk and hence the correlation of X-ray and optical flux is not expected from the observations dating before 2000, relevant time scale for this is the duration in which the radius of the outer disk matches to that of truncation and is evaluated as $\sim \frac{12}{(\alpha/0.2)}$ yrs after the disk formation for a standard viscous Shakura-Sunyaev disk (Lutovinov et al. 2012). According to Telting et al. (1998), there has been a diskless state of X-Per around 1990 when X-ray luminosity first peaked and then slowly diminished.

The source's overall variability peaks between 1987 and 2001. Above mentioned fluctuations seen in the emission from optical band hosts the variation of H_{alpha} and He I lines periodically in a time interval of 1 to 10 years. Absence of a correlation between line strength and emission coming from the continuum implies that the decretion disk goes through a redistribution of plasma within it, which adjusts the density gradient in the radial direction. As assumed, optical luminosity rise has almost no effect on X-ray luminosity before 2002. Re-appearance of the correlation between these two observables suggests that after 2002, compact object begins to interact with the completely restored equatorial disk. Starting from 2002 up to 2011, optical brightness remains in a relatively high value except for a small decrease in 2010, while X-ray luminosity has a little dip in between 2003-2004 which is attributed to the loss of outer portions of the disk, however it never drops to low values seen before 2002. Conclusively, it can be stated that X-Persei has been in a strong outburst activity starting from 2001 up to 2011 with an X-ray luminosity of $L_x \simeq 1.2 \times 10^{35}$ erg/s that is the maximum value for the last 30 years (Lutovinov et al. 2012).

As previously mentioned, X-Persei is a persistent source unlike most of the be type X-ray binaries and source's persistent X-ray emission is thought to be emanating from its nearly circular orbit. Bildsten et al. 1997 have determined the eccentricities of five Be/X−ray binaries, average being stated as $e\sim0.4$. Reig 20011 states that there are currently five BeXB (X Per, GS 0834−430, KS 1947+300, XTE J1543−568, and 2S 1553−542), characterized by $P_{orb} \sim$ 30 days and very low eccentricities ($e\sim0.2$). With an eccentricity of $e\sim0.11$, X-Persei system clearly has one of the most circular orbits among the other

systems in its class. A Monte-Carlo study examining natal kicks caused by the supernova explosions forming the compact object in the binaries was carried out by Delgado-Marti et al. 2000. According to this work, there is a tiny probability (around 1%) of finding the orbit with an eccentricity equal to or smaller than 0.11 after a supernova explosion. Currently there is no scenario to account for this orbit, yet it is that evident some neutron stars receive a much lower kick than their counterparts at their birth than previously accounted for by evolutionary models (Pfahl et al. 2002).

Due to the nearly circular orbit of X−Per, compact companion never goes through the decretion disk and the only accretion source seems to be the powerful but irregular stellar wind of the Be star. The compact companion orbiting relatively far away from the equatorial disk results in the absence of Type 1 outbursts at periastron for this source that are common for BeXRBs (Doroshenko et al. 2012). However, spectral changes indicate that a temporary accretion disk forms around 4U 0352+309 from time to time via capture of material from the wind. No major outburts are observed for this source and even during an outburst X-ray luminosity remains relatively low. An α value of 0.2 has been determined for the Shakura Sunyaev disk of X-Per system which enables the truncation of this disk by the neutron star. Viewing from a qualitative approach, low luminosities are accounted for when the neutron star is visioned to accrete from the outer regions of the circumstellar disk most of the time in which the truncation of the disk caused by the compact object also plays a role. Since the neutron star deos not intersect the dense inner regions of the disk, persistent low luminosity is an expected consequence of a circular orbit where two companions are wide apart. In this orientation, there is little material accreted and the neutron star is slowly rotating with a relatively weak magnetic field, as observed for all persistent BeXRBs. The small increases in X-ray emission about ten times the luminosity during quiescence are not comparable to flaring events observed for BeXRBs with eccentric orbits and these events may occur due to the mass ejections from the donor companion (Reig and Roche 2008). Furthermore, observational data is in accordance with the viscous decretion disk theory for Be stars (Clark et al. 2001). As it is common for many accreting X-ray pulsars,

both spin-up and spin-down trends are seen in the pulse period history of X-Per. Long term analysis of the pulse period indicate that the source was spinning up prior to 1978 with $\frac{\dot{P}}{P} \simeq -1.5 \times 10^{-4}$ 1/yr. This spin up trend was superimposed on erratic short term ($\sim$ few days) variations in pulse frequency. Observations after 1978 show that the neutron star experienced a large appearent torque reversal around 1987 and is spinning down with a similar rate $\frac{\dot{P}}{P} \simeq 1.4 \times 10^{-4}$ 1/yr since then. Pulse period behavior of the source is not studied carefully on short time scales. During the diskless state in 1990, brighter X-ray luminosity persisted about 6 years during which spinning up of the pulsar was observed as well. At the end of this spin-up phase, spin period increased. However during another diskless state at 1990, no spin-up behavior was observed. Because of the outburst between 2001−2011, spin-down trend observed from the source in prior 35 years changed to spin-up behavior with $\frac{\dot{P}}{P} \simeq -3.6 \times 10^{-4}$ 1/yr, which implies a greater acceleration than the previous spin-up/down trends of X-Per. It is suggested that the spin-up of the neutron star is dependent on the accretion flow hence the X-ray flux and can be explained with the Quasi-Spherical Accretion Theory of Shakura et al. 2012 (Lutovinov et al. 2012).

X-Per shows spin-up spin-down trends without any significant variations in the X-ray luminosity. The lack of a correlation between L_x and $\frac{\dot{P}}{P}$ implies that these changes cannot be related with the transitions between accretor and propeller regimes. A recent paper published at 2012 by Doroshenko et al. have concluded that although X-Per has a low X-ray luminosity for standard HMXBs, its luminosity is three orders of magnitude higher than what is expected for an accretion from a fast ($\sim$800 km/s) stellar wind with low density. The observed luminosity can be explained with a scenario where there is accretion from a slow ($\sim$150 km/s) and dense wind expanding from the equatorial disk of the donor star.

CHAPTER 4

OBSERVATIONS AND DATA ANALYSIS

4.1 Observations of X-Persei with RXTE

This work made use of the archival data collected by Rossi X-ray Timing Explorer (RXTE). RXTE was launched on 30 December 1995 and was decomissioned on 5 January 2012 after successfully covering its mission targets. The satellite has two pointed instruments, namely PCA (Proportional Counter Array) which covers the low energy ranges between 2-60 keV and HEXTE (High Energy X-ray Timing Experiment) which is designed to explore high energy ranges between 15-250 keV in X-ray band. RXTE also nestles a wide field device, the All Sky Monitor (ASM). X-Persei has 148 pointed observations from 6 different proposals with exposure times varying between 2 ks to 15 ks gathered by the PCA instrument of the satellite. PCA hosts five proportional counters amounting to a total collecting area of 6500 cm^2. Its energy range is 2-60 keV with a resolution better than 18% at 6 keV. PCA has a time resolution of 1 microsecond and a spatial resolution of 1 degree FWHM. The detector is consisted of 1 Propane veto layer, 3 Xenon layers (with each split into two) and 1 Xenon veto layer. RXTE PCA has operated with some proportional counter units turned down in order to extend the lifetime of the device[1].

[1] http://heasarc.gsfc.nasa.gov/docs/xte/rxte.html

Table4.1: RXTE-PCA observation list for X-Per.

Proposal ID	Exposure (ks)	Number of Pointings	Time (MJD)
30099	252	56	50995 − 51406
40424	60	14	51420 − 51597
50404	58	12	51634 − 51940
60067	398	58	52000 − 52687
60068	25	8	52094 − 52398

4.2 Discovery of Quasi-Periodic Oscillations

X−Persei was observed by RXTE in the time interval between 01.07.1998 and 17.02.2003 with frequent gaps between observations. Lightcurves of the source were extracted making use of all the data available from RXTE in the energy band 3-20 keV. Even a superficial look at the light curve shows that the X-ray luminosity increases starting from about MJD 51920 which is the middle of the full observation time, having a maximum value at the end of the ligthcurve.

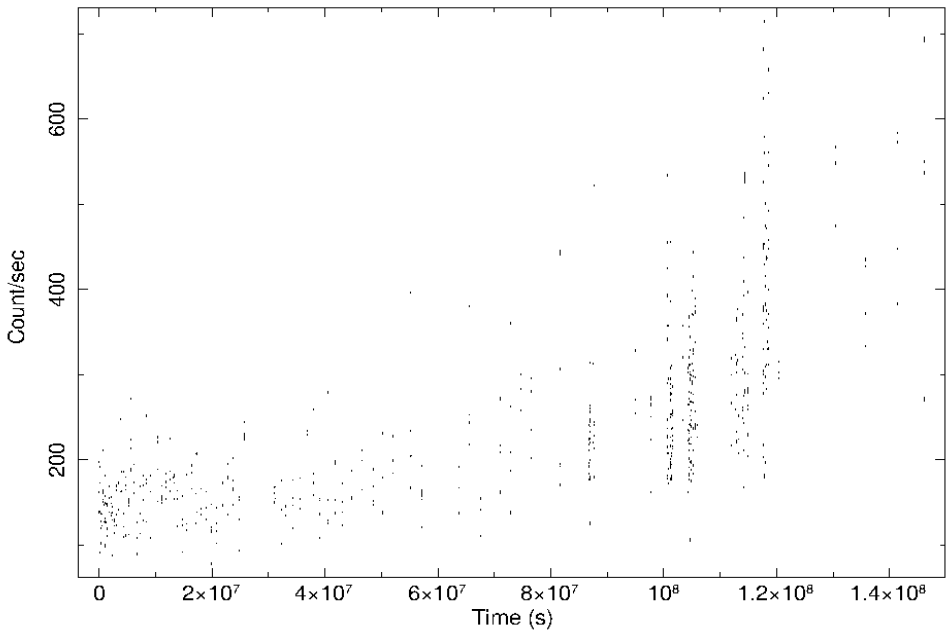

Figure 4.1: RXTE-PCA lightcurve of X-Per in the energy band 3-20 keV.

Table4.2: Details of the power excess fits.

Epoch (MJD)	Frequency (Hz)	FWHM (Hz)	F-test σ	Q value	RMS amplitude
51258	0.028±0.013	0.01±0.009	1.65 σ	2.946	8.236
51754	0.078±0.012	0.009±0.006	2 σ	8.599	4.735
52205	0.031±0.012	0.015±0.006	1.65 σ	2.115	6.089
52212	0.035±0.014	0.035±0.012	3.2 σ	2.21	5.015
52315	0.038±0.014	0.012±0.009	1.65 σ	3.235	6.866

It can be safely assumed that the source entered in an outburst during the observations and was still increasing in luminosity when the RXTE observations stopped.

The search for aperiodic variability and quasi periodicities were conducted by the use of each observation group's own lightcurve. Three lightcurves were produced for each observation in different energy bands. fter a visual check of the power spectra obtained from 3−10 keV, 10−20 keV and 3−20 keV lightcurves of each observation it is concluded that X-Per's overall power spectral behavior

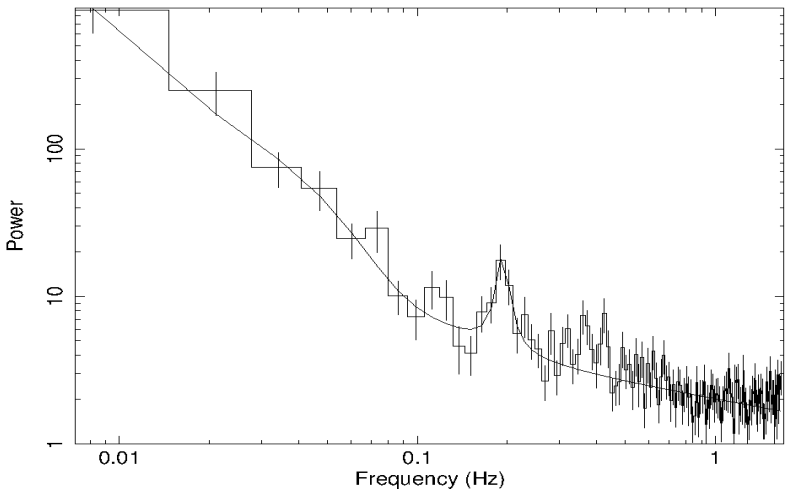

Figure 4.2: PDS of MJD 51060.

can best be represented by 3−20 keV PDS where fluctuations also have higher significances.

Lightcurves were produced with 0.1 s time resolution and PCA Good Xenon Event data were used. These lightcurves were corrected for PCU times, after the barycenteric corrections were made and the background lighcurves were subtracted. For X-Per, the background suitable for faint objects was used, which is provided by the RXTE team. Data from all available PCUs were used in this analysis. These data are chosen such that during these observations, the elevation angle is greater than 10° and the offset from the source is less than 0.02° whereas the electron contamination of PCU2 is less than 0.1. Data reduction and analysis were carried out using the standard `HEASOFT v.6.13` software tools.Some custom made tools with the tools from Markwardt Library [2] were made use of in the Interactive Data Language for the detailed investigation and statistical evaluation of the QPO candidates. Curve fitting was made with the use of the fitting tools inside PLT/QDP. The default non-linear curve fitting program inside QDP is Curfit which uses the Levenberg-Marquardt Algorithm for the minimization problem in non-linear least squares fitting (Tennant 1990).

Power spectra of each lighcurve was produced with 307.2 seconds time segments (with 0.3 seconds newbin time and 1024 seconds per frame) using Leahy normalization (Leahy et al. 1983). Frequencies were rebinned 4 times and 2 or 4 consequent frames were collected to produce power spectra. The resulting PDS were examined dynamically, which also revealed some insight about time dependent variability of the fluctuations. The frames that were found worthy of statistical analysis were picked out of the sequential PDS (power density spectra) windows. After obtaining the relevant chi−square values for the fits, F-test is used to estimate the significance of the peaks. Craig Markwardt's IDL code MPFTEST was implemented in the F−Test script to calculate probabilities. This code compares the value drawn from an F-distribution to a given value of F, which is later used for testing the level of confidence of detections. MPFTEST takes an F value and the degrees of freedom for the first and the second fits as inputs. In turn, it returns a scalar or a vector of probabilities

[2] http://www.physics.wisc.edu/ craigm/idl/

making use of an incomplete beta integral. The F ratio is taken as follows,

$$F_1 = \frac{(\chi_1 - \chi_2)/(d_1 - d_2)}{\chi_2/d_2} \tag{4.1}$$

as suggested by the author of the script. Here χ_1 and χ_2 are chi-squared values before and after model fitting and d_1 and d_2 are the degree of freedoms without and with the model (Markwardt 1999). As can be seen, this ratio requires the estimations of χ^2 values of each fit as well as their degrees of freedom. Calculation of the χ^2 values were carried out using the standard chi-square method which is implemented in the F-test script. Differences between the expected and the observed values (residuals) were determined by subtracting the simulated best fit data from the original data. Chi-square calculation uses the instrumental errors caused by satellite/measurement insufficiencies taken from PDS as variances.

X-Per has a quite irregular lightcurve and the erratic changes in it can be seen in its PDS as well. It is a well known fact that HMXB power spectra contain lots of bumps and wiggles which makes them hard to describe with simple analytical laws as in LMXB (Reig et al. 2013). X-Per follows the same trend and it is striking that only a very small number of the power spectra produced in this process could be fitted with a double power law, P_{tot} model,

$$P_1 = A \times \upsilon^b \tag{4.2}$$

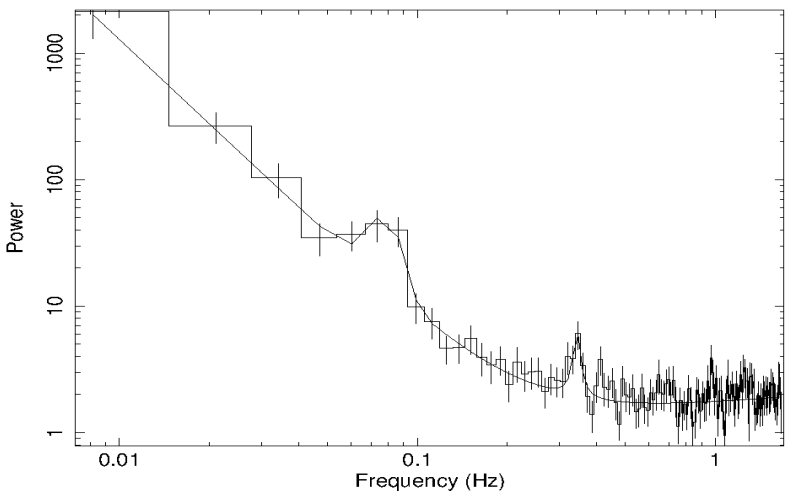

Figure 4.3: PDS of MJD 51754.

$$P_2 = C \times \upsilon^d \tag{4.3}$$

with

$$P_{tot} = P_1 + P_2 \tag{4.4}$$

without the need of extra components. The remaining spectra are various in their features, yet they can be generally classified. At frequencies lower than 0.1 Hz, there are lots of broadband fluctuations changing frequencies with time, while at frequencies higher than 0.1 Hz, there is a prominent activity between 0.1 and 0.4 Hz.

In this thesis, quasi-periodicities around frequencies in between 01 to 0.4 Hz are reported. It is seen that the QPO feature shifts between ∼0.1 and ∼0.4 Hz, with the most significant appearances being on 0.1 and 0.2 Hz. Most prominent feature below 0.1 Hz is the nearly permanent power excess at lower frequencies. This feature appears between 0.01-0.02 Hz at the beginning of the lightcurve and gradually shifts in frequency with time, up to frequencies ∼ 0.07-0.08 Hz. This excess can be observed in almost 90% of the power spectra produced, so it can be assumed that it is a fairly permanent fluctuation in the lightcurve of X-Per and is an intrinsic property of the source's X-ray brightness due to its accretion flow. Other HMXB sources, such as Cen X-3 also exhibit these particular noise features (Belloni & Hasinger, 1990).

Low frequency noise of X-Per modifies the PDS below 0.1 Hz in frequencies mainly in between 0.02 Hz and 0.08 Hz. Activity in the mentioned frequency range has been previously discussed in Takeshima 1998, where a 0.054 Hz QPO feature has been reported. In our current analysis of RXTE data however, the activity in this range is seen only as broad noise components, which are strong with high RMS amplitudes yet have low Q values to be considered as QPOs.

Power spectra have been visually checked for the appearance of spin period and its harmonics. Normally, they are expected to be seen as narrow peaks. Widths of the pulse harmonic bins depend on the frequency resolution which in turn depends on the choice of time segments used in producing the power spectra. Since the power spectra have been divided in time segments of 307.2 seconds,

Table4.3: Detected QPOs.

Epoch (MJD)	Frequency (Hz)	FWHM (Hz)	F-test σ	Q value	RMS amplitude
51049	0.1 ±0.012	0.017±0.015	2.6 σ	6.04	4.43
51060	0.195 ±0.012	0.019±0.01	3.5 σ	11.92	4.26
51258	0.095 ±0.015	0.006±0.003	1.3 σ	16.77	4.73
51754	0.343 ±0.07	0.019±0.011	3.3 σ	17.99	1.88
52205	0.1 ±0.016	0.002±0.001	1.7 σ	58.64	0.98
52211	0.223 ±0.014	0.004±0.002	1.7 σ	63.40	4.75
52212	0.195 ±0.012	0.005±0.001	2 σ	32.60	2.69
52217	0.197 ±0.012	0.014±0.012	2 σ	14.28	2.87
52315	0.108 ±0.018	0.01±0.003	2 σ	20.61	2.63
52316	0.147 ±0.01	0.012±0.006	2.5 σ	11.88	3.69
52368	0.119 ±0.01	0.017±0.008	2.6 σ	7.14	3.26
52687	0.095 ±0.013	0.015±0.005	2.5 σ	6.56	6.09

pulse and its harmonics should have 0.00325 Hz approximate width, that is, if they can be detected in the spectra (Reig 2008). In the case of X-Per, there is no appearance of harmonics above 0.1 Hz. Pulse itself can be seen clearly in one bin at around 0.0012 Hz, however, the appearance of its harmonics are not so clear and permanent all the time. Since the QPO frequencies remain unaffected

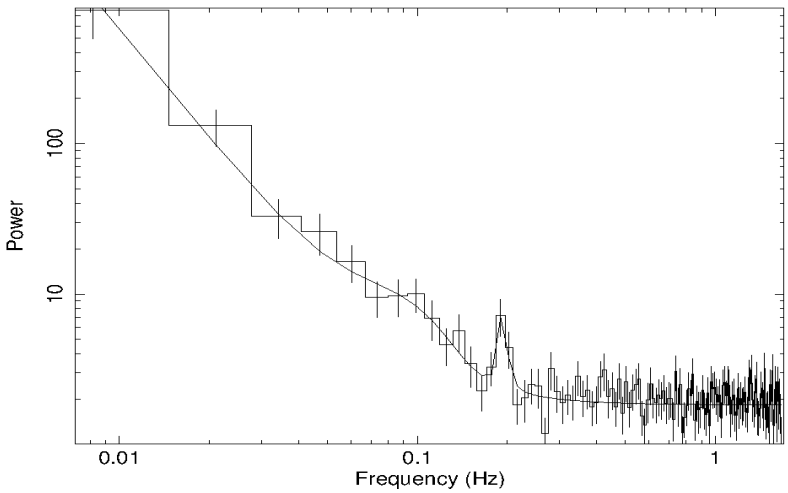

Figure 4.4: PDS of MJD 52212.

from pulse harmonics, they haven't been removed from the power spectra while examining the quasi−periodic features. The 4^{th} pulse harmonic at 0.0192 Hz which has a width of 1.356×10^{-2} Hz could be contributing to the excess at 0.02 Hz, however this excess is one order of magnitude broader than is expected from a harmonic feature as well as its temporal changes are visible during the dynamical examination of the power spectra. This implies that the harmonic is not the main/only component that creates this excess and there might be a meaningful process governing this phenomenon.

In the light of the explanations above, all PDS created were fitted with a default double power law, an excess component modeled with a Gaussian if necessary and either with a Lorentzian or a Gaussian component for the QPO.

Gaussian fit relation is,

$$f_G = GN \times e^{\frac{-Z^2}{2}} \tag{4.5}$$

with

$$Z = \frac{X - GC}{GW} \tag{4.6}$$

where X are the frequencies, GN = Gaussian line normalization, GC = Gaussian line center and GW = Gaussian line width.

A Lorentzian fit is defined as,

$$f_L = \frac{LN}{1 + \left(2 \times \frac{X-LC}{LW}\right)^2} \tag{4.7}$$

where X are the frequencies, LN = Lorentzian line normalization, LC = Lorentzian line center and LW = Lorentzian line width.

The choice on the QPO model was made according to the best fits, which can also be verified by visually checking the accordance of the shape of the model to the actual peak. Decision on the existence of the excess component was made according to the significance of the Gaussian fit.

Information on all QPOs are given in Table (4.3) with details. PDS and lightcurves of the observations with QPO detection can be found in Appendix 1.

Table4.4: Mean count rate and flux values of regions with QPO activity.

Epoch (MJD)	Mean count rate (count/sec)	Flux (ergs/sec.cm^2)
51049	103.038	2.84×10^{-10}
51060	227.975	4.06×10^{-10}
51258	107.0156	2.74×10^{-10}
51754	362.494	4.13×10^{-10}
52205	299.994	4.66×10^{-10}
52211	313.950	5.63×10^{-10}
52212	173.384	4.42×10^{-10}
52217	288.896	5.99×10^{-10}
52315	233.079	5.29×10^{-10}
52316	271.241	5.02×10^{-10}
52368	514.958	8.14×10^{-10}
52687	524.541	1.30×10^{-9}

4.3 X-Per's Broad-Band Power Spectra

Another way to effectively study the power spectra of an X-ray source is, instead of using smaller segments as in QPO search, to average larger segments of the observations and investigate the variabilities on these time-scales. Since QPO features cannot be detected in every HMXB source due to their temporary appearance in power spectra, determination of the behavior of the accretion flow via the analysis of data from broad time intervals is often convenient (Revnivstev et al. 2009).

Around ten different X-ray binaries have been studied in Revnivtsev et al. 2009 for the trends in their broad band power spectra. An overall investigation of these accreting binaries revealed that most of these sources exhibit a break in their PDS close to the compact object's spin frequency. This break frequency is interpreted as the transition from disk flow to magnetospheric flow at the disk truncation radius. Break frequency closely follows the local Keplerian frequency at the truncation radius. If the disk and the compact object are in corotation, the break frequency is equal to the spin frequency and the variations are seen

in the Keplerian time-scale as it is with the case of no corotation.

Authors suggest the "Perturbation Propogation Model" as an explanation of this power spectral trend. This model explains the variability in the source X-ray luminosity as the perturbations in the accretion disk, caused by stochastic events. Instantaneous disturbances in the inner accretion flow travel with the help of the viscous stresses in the disk to the region where most of the X-ray emission is released and become variations in the X-ray luminosity as they radiate their energy. Combination of these small perturbations are seen as a power law with index -1 to -1.5 in the power spectrum. In this picture, an outburst in the source luminosity is directly related to the increase in the mass accretion rate, resulting in a decrease at the magnetosphere size which can be observed in the PDS as an increase of the break frequency. Here, a change in accretion rate means a change in the X−ray luminosity, which disrupts the corotation and adjusts the place of the break in the frequency domain. According to the model, the edges of the accretion disk in a system contributes to the noise features of X−ray binaries, introducing a break frequency at the inner edge whereas the slope changes in the power law is related to the magnetospheric effects towards the outer edge.

Another aspect of noise features in the broad band power spectra is its relation with quasi−periodic oscillations. Since QPOs are observed from the inner parts of an accretion disk, near the inner edge, correlations are expected between signatures of disk edges in the power spectrum and QPOs. In some LMXBs, the interrelationship of QPOs and break frequencies have been observed. In this perspective, it makes sense to search for these correlations in the case of X−Persei as well. In this model, Keplerian frequency at the magnetospheric radius R_m is expressed as,

$$2\pi\upsilon_K = (GM)^{1/2} R_m^{-3/2} \tag{4.8}$$

with magnetospheric radius being,

$$R_m \approx \mu^{4/7} (GM)^{-1/7} \dot{M}^{-2/7}. \tag{4.9}$$

Then the break frequency is defined as,

$$f_b \propto \upsilon_K \propto (GM)^{-1/7} \dot{M}^{3/7} \tag{4.10}$$

Table4.5: Broken power law fit parameters for two broad-band spectra. f_1 and f_2 are first and second break frequencies respectively.

Obs. ID	Const.	f_1	1^{st} Indice	f_2	2^{nd} Indice
P30099	74.39(±18.2)	$7.06(\pm1.6)\times10^{-4}$	1.28(±0.04)	$2.25(\pm0.2)\times10^{-2}$	2.07(±0.04)
P60067-2	71.44(±8.6)	$9.34(\pm0.8)\times10^{-4}$	1.405(±0.03)	$2.36(\pm0.1)\times10^{-2}$	2.031(±0.02)

Two broad band spectra were produced to examine X−Per's power spectral properties. Lightcurves obtained from observations with proposal ID 30099 (between MJD 50995 and MJD 51406) and a part of observations with proposal ID 60067 (between MJD 52208 - MJD 52687) are used to produce these two power spectra. Splitting the whole lightcurve into two broad spectra is avoided, because of the irregular gaps between observations, especially on the second half of the RXTE data. This is not a drawback since two broadband spectra generated from observations P30099 and P60067 demonstrate the behavior of their broader counterparts. Spectra are normalized such that the integral over the PDS gives the squared fractional RMS amplitude (Miyamoto et al. 1991). The bin corresponding to the pulse frequency has been removed in both of the power spectra created.

These two broad-band spectra were fitted with a double break model (Revnivtsev et al. 2009). This model takes five input values (P_1,P_2,P_3,P_4,P_5). Two break frequencies are given to the model to ascertain the breaks in the spectrum. Remaining three values determine the behavior of the power law functions in between these break points. In this case, interval before the first break point takes a constant value of P_2 because of the dominance of white noise in lower frequencies. After the first and second breaks, two power law functions $f_1(x) = P_2 \times x^{P_3}$ and $f_2(x) = P_2 \times x^{P_5}$ are sufficient to describe the spectrum respectively, where two break values in the frequency domain, $f_1 = P_1$, $f_2 = P_4$ are given. The spectra and their fit parameters are shown in Table (4.5).

Beginning of this data corresponds to a standard luminosity for X−Per, with $L_x = 2.35 \times 10^{34}$ ergs/s with relevant flux being derived from energy spectral fit of the P30099 data set. For this basic approximation, Cflux model of XSPEC have been used, which required fitting wabs×(bbodyrad+pow) models first (Lu-

tovinov et al.2012). The same procedure revealed a flux value three times higher for the second part of the P60067 data set, corresponding to $L_x = 7.04 \times 10^{34}$ ergs/s.

Revnivstev et al. state that break frequency is directly related to the mass accretion rate and the luminosity. X-Per is not an exception and the first break frequency increases with the increase of the X-ray luminosity. However, no significant change is observed for the second break frequency of the source. Revnivtsev et al. have examined their sources with a coarser time resolution and hence suggested that they obey the relation,

$$P \propto f^{-1} \left(1 + \left(\frac{f}{f_0}\right)^2\right)^{-0.5} \tag{4.11}$$

with only one break point, where f_0 is the pulse frequency. X-Per's less broader PDS clearly shows double break points, with one being at the neutron star spin frequency, as the authors suggested and the other being at $\sim$0.01 Hz, which might indicate an interaction between a possible accretion disk and the magnetosphere. It should be pointed out that with a keener look at the overall plot (Fig.1 of Revnivtsev et al. 2009) it is not hard to see the double break behavior at the frequency domain both for X-Per and some other sources as well. It has been discussed by several authors previously in detail that any kind of inter-

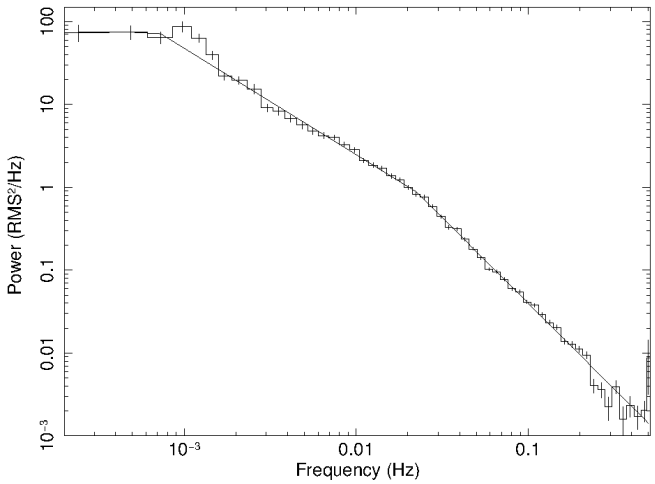

Figure 4.5: Broad-band PDS of P30099.

action between the disk and external conditions should take place with a time scale corresponding to the viscous time scale of the disk at the relevant radius. Viscous time scale of the disk is the time conforming to the transfer of matter in the accretion disk,

$$t_{disc}(R_d)^{-1} \sim f_{break} \tag{4.12}$$

with the longest time scale possible for an accretion disk being that of its outermost boundary. Variations lower then this specific frequency are uncorrelated with the flow and hence interpreted as white noise, seen in the spectra as a flat continuum below the break frequency. High frequency fluctuations are seen as the result of the mass accretion rate changes coming from the inner parts of the accretion disk which is the region responsible for energy generation/ X−ray emission. On the other hand, mass accretion rate fluctuations formed at the outer parts of the disk are seen in the low frequency domain of the PDS. They form at the outer edges of the disk and evidently, they travel through the accretion disk all the way up to the energy generation region. Since a Shakura−Sunyaev disk actually acts as a low pass filter, it transmits only the fluctuations with longer time scale than that of the local viscous time. Naturally, regarding the outer parts of the accretion disk, only low frequency fluctuations can be seen in the PDS. If an accretion disk harbors different flow components at different radii with distinct time scales, each will be seen as separate breaks in PDS

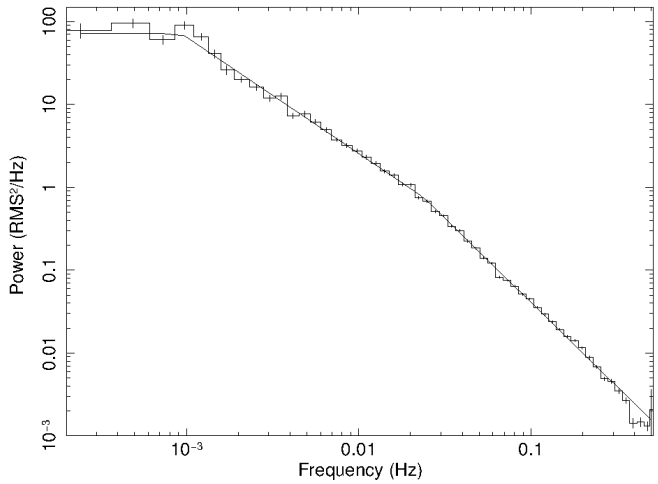

Figure 4.6: Broad-band PDS of P60067.

corresponding to the inverse of the local time scale for these components. The overall shape of a source's PDS continuum depends on the contributions of separate $\dot{M}$ fluctuations due to different components and behavior of the donor star (Gilfanov and Arefiev et al. 2005).

4.4 Hardness-Intensity and Color Diagrams

It is of importance to put X-Per's aperiodic variability patterns in a broader picture by analysing the emission of the source in different energies. This provides one with a meaningful insight about the origin of photons in different times. An expectable behavior for an accreting X-ray binary would be that as the flow patterns change (ie. parameters controlling the matter flow onto the compact object, like the velocity of the stellar wind) the geometry and size of the emission region change as well. This would cause the observer to detect different energy photons with different count rates in time. For this kind of work, two basic diagrams involving data from lightcurves from different energy bands but same time intervals are commonly used. A hardness-intensity diagram (HID) consists of lightcurves from two separate energy bands. In the x-axis, sum of the count rates are shown while in the y-axis the ratio of two series are plotted. A color diagram, in which a total of four energy bands are involved, is more comprehensive. X and y axes of a color diagram consists of the ratio of count rates in different energy bands respectively, traditionally a ratio of softer and another ratio of harder parts of the energy spectrum plotted against one another.

For reasons explained in the previous chapter related to QPO analysis, energy range of 3-20 keV has been selected to investigate X-Per's power spectra. Lightcurves were extracted with 16 seconds time resolution from Standard 2 data where only the data from PCU2 were used. These lightcurves were then binned with 2511 second time intervals that correspond to a duration of 3 pulses. 3-7 keV and 7-10 keV lightcurves were used for soft part HID, while using 10-15 keV and 15-20 keV lightcurves for the harder segment. All four lightcurves were used to produce the color diagram. In order to fully comprehend the trend in photon energies, the output data were divided in 8 time intervals. This division

Table4.6: Time intervals and symbolizations for CID and HIDs.

Group number	Epoch (MJD)	Observation ID	Symbol
1	50995-51195	P30099	Big star
2	51195-51406	P30099	Star
3	51420-51597	P40424	Circle
4	51634-51939	P50404	Cross
5	52000-52129	P60067-P60068	Square
6	52129-52258	P60067-P60068	Triangle
7	52258-52388	P60067-P60068	Circle with cross
8	52388-52687	P60068	Diamond

was made according to the observation times when possible. Time intervals used can be seen in Table (9.3). The lightcurves used to produce these diagrams can be found in Appendix 2.

Soft HID consists of two branches. The first branch at the bottom left of the diagram has the lowest ratio of 7-10 keV to 3-7 keV lightcurves with values ranging between 0.25 to 0.35. This part consists of the softest photons in the

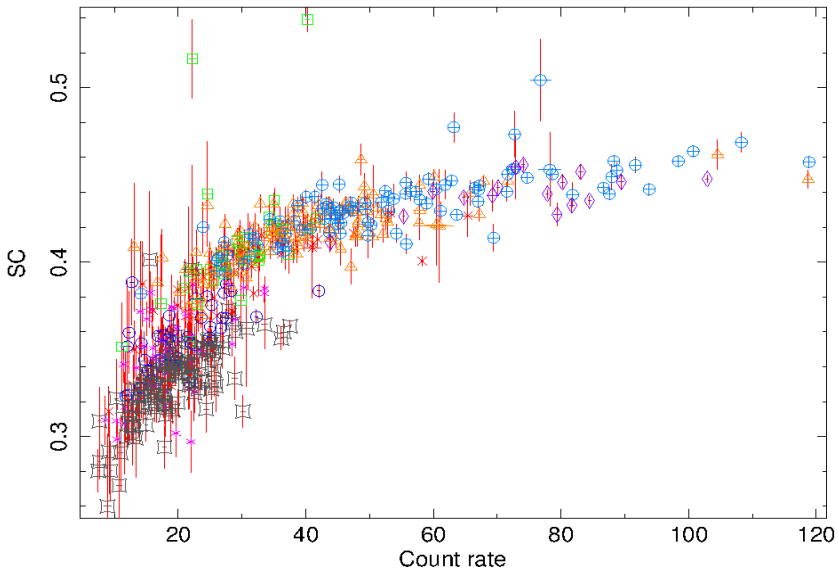

Figure 4.7: Hardness-intensity diagram for soft color (3-7/7-10 keV). Grey (big stars), magenta (stars), dark blue (circles), red (crosses), green (squares), orange (triangles), blue (circles with cross) and purple (diamonds) markers indicate group 1 to 8 in Table 4.6 respectively.

soft photon regime and coincides with the observation sets P30099, P40424 and P50404. In these sets, QPO frequencies are in the range ∼0.095 to ∼0.35 Hz. The second branch in the diagram spans the ratio values of 0.35-0.55. This branch coincides with the increase of the count rate of the source. Observations from P60067 and P60068 occupy this region of the diagram. As the count rate increases, this branch becomes the only one still visible on the diagram. This means that as the source enter its outburst, energies of the soft photons increase. It can be discussed that as the source luminosity increases, it is no longer possible to see softer photons due to some geometrical constraint and/or this outburst corresponds to a change in the disk which results in the emission of harder photons. QPO frequencies on this branch are in the range 0.099-0.269 Hz. The softest spectral region is occupied by a few data points around 0.3 and below. Immedietaly after this softest period, the highest frequency QPO is seen during the observation P50404 with a frequency of ∼ 0.35 Hz. The time evolution of the diagram can be inferred from the labels. Photons in the respective observations, starting from a harder energy, get softer in time until the observation set P40424

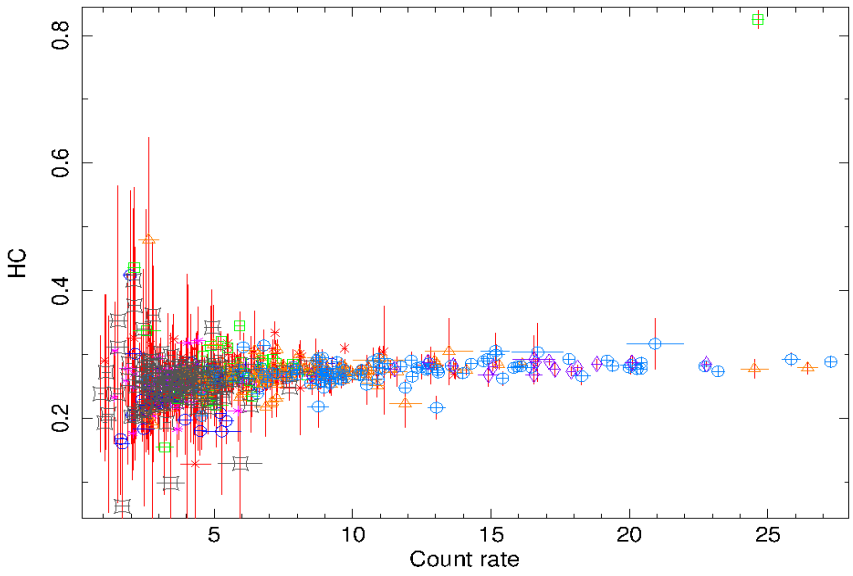

Figure 4.8: Hardness-intensity diagram for hard color (10-15/15-20 keV). Grey (big stars), magenta (stars), dark blue (circles), red (crosses), green (squares), orange (triangles), blue (circles with cross) and purple (diamonds) markers indicate group 1 to 8 in Table 4.6 respectively.

after which they harden and remain with a quite constant photon energy at the end (around 0.45), regardless of the significant raise in the count rate. It is worth noting that until to the end of observation P50404, X-Per remains in a spin-down state. At about MJD 52120, source switches from spin-down to spin-up, which is observed as an hardening in the energies of soft photons. Up to the color value of 0.4, the photos remain in relatively soft energies. However, with the flip of the spin behavior, photon energies start to increase, which also corresponds to the start of the outburst.

Hard HID consists of one branch with only a few scattered points that cannot posit great significance. It can be seen that the variability in soft energies is not accompanied by a variability in hard energies. Softest photons are emitted from P30099 to P50404. The overall color value of the hard photons is around 0.3.

Color-color diagram of the source neatly summarizes the variabilities in 3-10 keV and the lack of variabilities in 10-20 keV. The whole island of points reveal the trend in the soft HID. This one branch is relatively constant at hard color

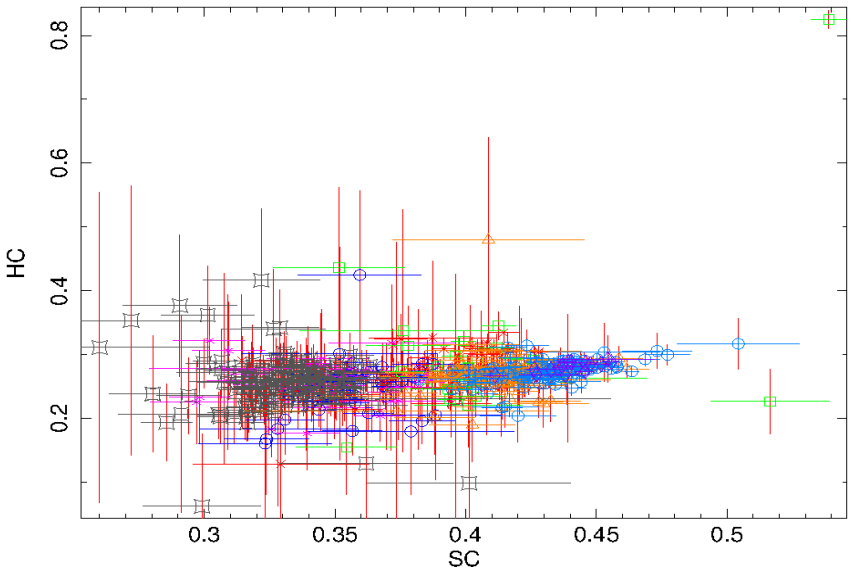

Figure 4.9: Color-color diagram for four energy bands. Grey (big stars), magenta (stars), dark blue (circles), red (crosses), green (squares), orange (triangles), blue (circles with cross) and purple (diamonds) markers indicate group 1 to 8 in Table 4.6 respectively.

while soft color values change with time. As the source goes into an outburst, the soft photons become harder, demonstrating a positive correlation with the X-ray luminosity.

4.5 Comments on Energy Spectra

Although this work is based on the detailed analysis of power density spectra, a small segment is reserved for discussing general energy spectral properties of X-Per, in order to complete the discussion on hardness-intensity and color diagrams. Energy spectrum of each observation set has been extracted with the FTOOLS package in HEAsoft, making use of the Standard 2 mode data which has 128 energy channels and 16 seconds time resolution. In producing the spectra, only data from PCU2 detector of RXTE satellite has been used, as recommended by the RXTE GOF. Energy range was chosen as 3 to 20 keV, as it has been the preference throughout this thesis. XSPEC program was used for spectral analysis. All spectra were analysed after applying a systematic error addition of 0.5%. All spectra were fitted with wabs×(bbodyrad+pow) model. It has been discussed that the addition of a cyclotron resonance absorption line with the use of a cyclabs or gabs model increases the fit significance (Lutovinov et al. 2012). However, for the basic discussion here, addition of this feature is avoided. Spectral parameters obtained for each observation are demonstrated in the Table (4.7), along with their respective χ^2 values.

Photon index averages around 2 when the whole RXTE data is considered. In smaller time segments, the observation sets in this case, variation of the photon index principally follows the trend in soft HID. Observations start with a relatively higher photon index, $\gamma = 2.05858$ with P30099, gradually decreasing up to 60067-part1, after which it slightly rises again to a value between 1.85-2.09.

It can be said that the initially harder emission of the source gets softer as the count rate increases, with the exception of last two observations, which coincides with the peak of the flaring event. Blackbody temperature also follows a similar trend and is increasing with the count rate. As mentioned in Lutovinov et al.

Table4.7: Best fit spectral parameters of each observation set.

Obs. ID	Blackbody Temp. (kT)	Blackbody Temp. Normalization	Photon Index	Photon Index Normalization	Reduced χ^2	D.o.f.
P30099	$1.55^{+0.0053}_{-0.0053}$	$1.16^{+0.025}_{-0.025}$	$2.06^{+0.004}_{-0.0035}$	$5.9^{+0.08}_{-0.08} \times 10^{-2}$	1.199	43
P40424	$1.56^{+0.0067}_{-0.0067}$	$1.46^{+0.032}_{-0.031}$	$1.95^{+0.0056}_{-0.0055}$	$5.8^{+0.09}_{-0.09} \times 10^{-2}$	1.486	35
P50404	$1.59^{+0.0064}_{-0.0064}$	$1.88^{+0.055}_{-0.052}$	$1.87^{+0.0044}_{-0.0043}$	$6.5^{+0.15}_{-0.15} \times 10^{-2}$	1.517	35
P60067−1	$1.58^{+0.0041}_{-0.0041}$	$2.11^{+0.051}_{-0.049}$	$1.82^{+0.0023}_{-0.0023}$	$6.9^{+0.14}_{-0.14} \times 10^{-2}$	1.615	39
P60067−2	$1.75^{+0.0063}_{-0.0063}$	$1.36^{+0.031}_{-0.030}$	$2.09^{+0.002}_{-0.002}$	$0.2^{+0.2}_{-0.2} \times 10^{-2}$	1.308	37
P60068	$1.63^{+0.027}_{-0.025}$	$2.13^{+0.200}_{-0.180}$	$1.85^{+0.03}_{-0.03}$	$7.9^{+0.54}_{-0.52} \times 10^{-2}$	1.751	35

n_H is taken as 3.4 $\times 10^{22}$ cm^{-2}.

2012, both the blackbody temperature and the normalization of the photon index increase with the increase of the intensity of the source. Although a complete separation of these effects is not possible, due to the results on hardness analysis of the source (which will be discussed in the next section), it can be speculated that the time intervals with abundant and diverse noise frequencies and increased soft emission actually coincide. This fact may support the argument that soft energy photon production mechanism is also a yielding process for significant

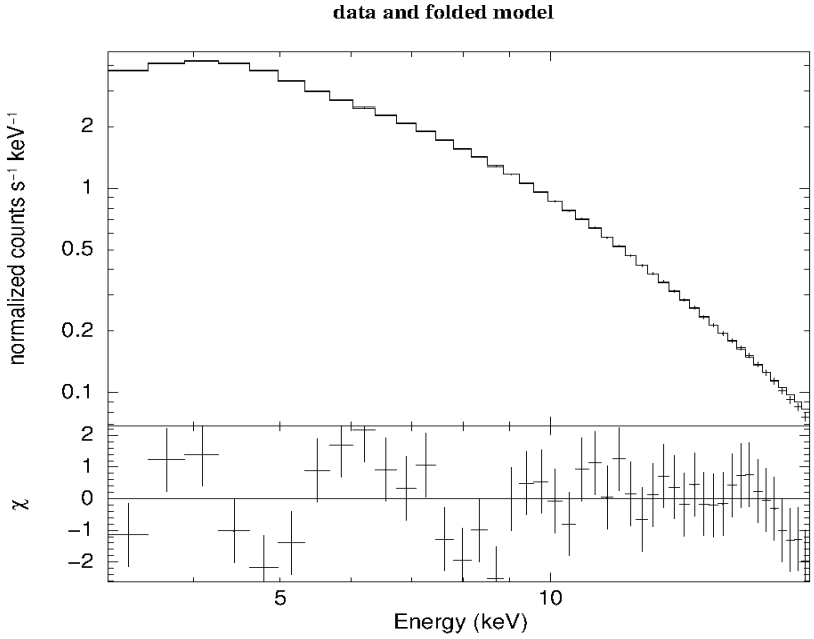

Figure 4.10: Energy spectrum, model fit and residuals for observation P30099.

quasi-periodic variability. Variation of the thermal components in small time intervals are discussed in Lutovinov et al. 2012 and they can also be seen in the relatively longer energy spectra investigated in this section. These variations are correlated with small flaring events and it is likely that these events modify the noise features in the PDS as well.

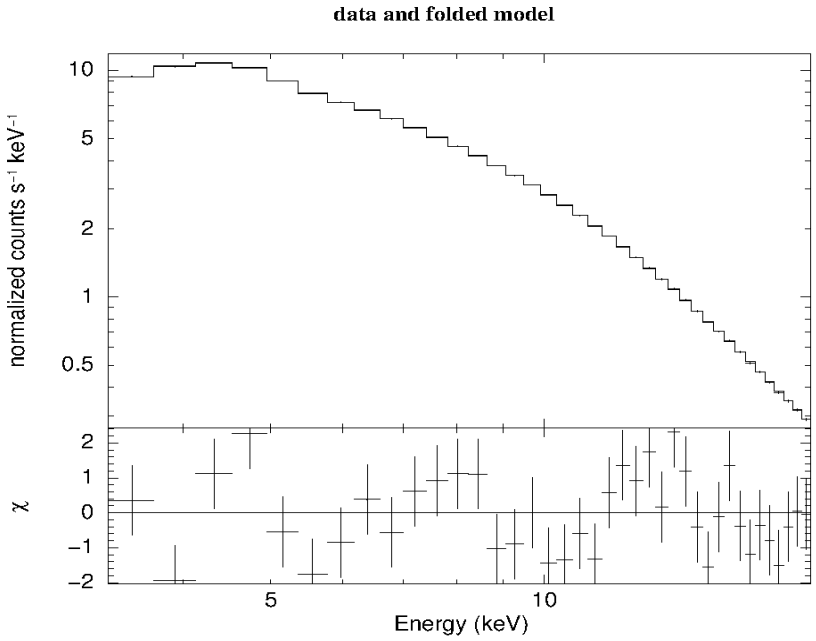

Figure 4.11: Energy spectrum, model fit and residuals for observation P60067 for the interval between MJD 52208 - MJD 52687.

CHAPTER 5

RESULTS AND DISCUSSION

5.1 Trends in QPO Behaviour

Line centers versus time In Figures (5.1) and (5.2), evolution of QPO and excess frequencies with respect to time can be seen. There exists no trend for neither QPO nor excess frequencies in that depends on time. Besides an evident peak at MJD 51754 and a subsequent drop following it, there is no indication that QPO frequencies increase with time, which would be expected according to KFM, since the source luminosity increases significantly approaching the end of RXTE data. The picture is quite similar for the excess frequencies. Figure (5.3) shows the ratio of QPO and excess line center against time. Trend of the ratio is similar to the trend observed when it is plotted against source flux. This is to be expected since, besides a short interval of higher flux values at the very beginning of the RXTE observations of X−Per, flux rises in time, as the source enters an outburst. The peak value of the ratio, corresponding to 51754 MJD takes place at a relatively low flux value when compared to the outburst flux values. As suggested by KFM or BFM, line centers of QPOs do not follow a positive trend with the source luminosity and this is seen in the behavior of QPOs with respect to time as well. Figure (5.4) shows a clear selection criteria for QPO frequencies depending on the source flux. Between 4 to 6 $\times 10^{-10}$ ergs/cm^2.s QPOs with frequencies 0.1 Hz up to $\sim$ 0.35 Hz can be observed. However, below and above these values, variety in the QPO frequencies suddenly vanish, leaving only frequencies around 0.1 Hz. This behavior might be correlated with the motion of the temporary accretion disk around the neutron star's magnetosphere. It

can be speculated that inside this relatively small interval of flux values, accretion around the compact object has a geometry that allows the disk to further

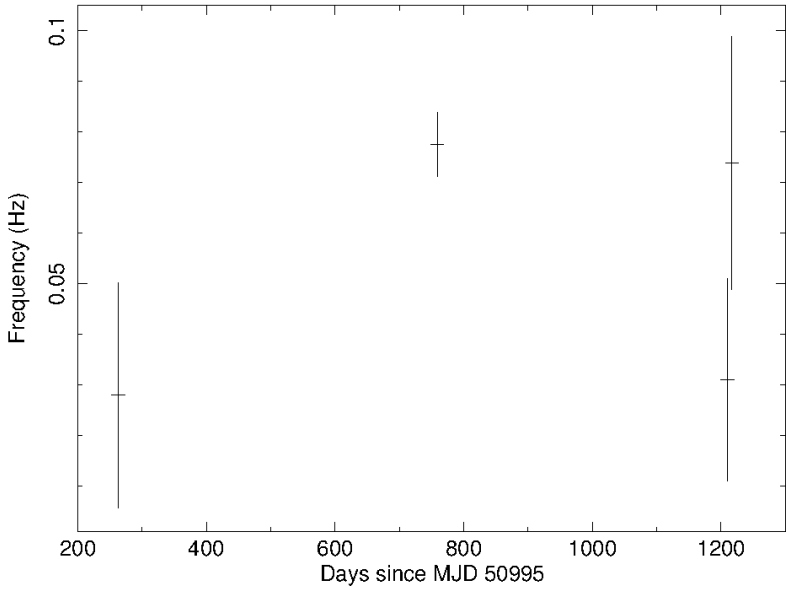

Figure 5.1: Excess frequency with respect to observation day.

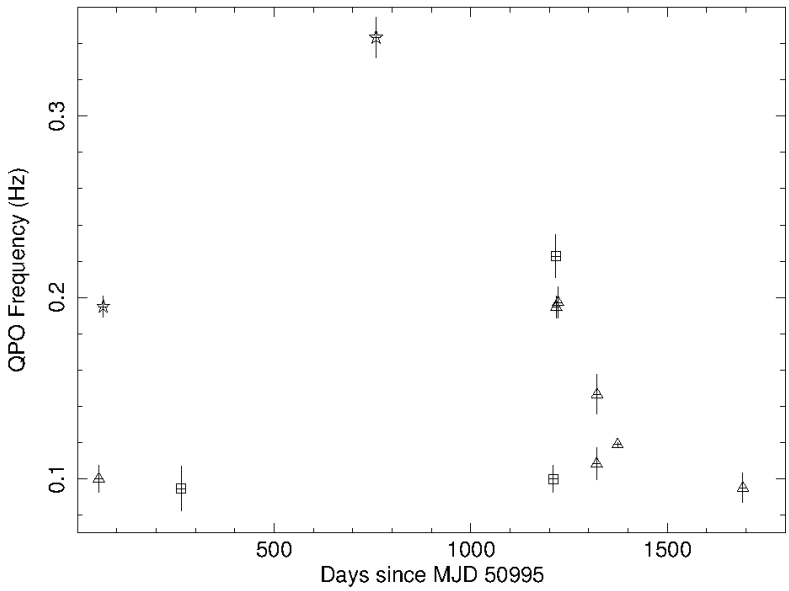

Figure 5.2: QPO frequency with respect to observation day. Stars are QPOs between 3-4σ detection, while triangles have significances between 2-3σ and squares have significances below 2σ.

penetrate the magnetosphere and get closer to the accreting object, causing an increase in frequencies observed, since they most likely represent the Keplerian

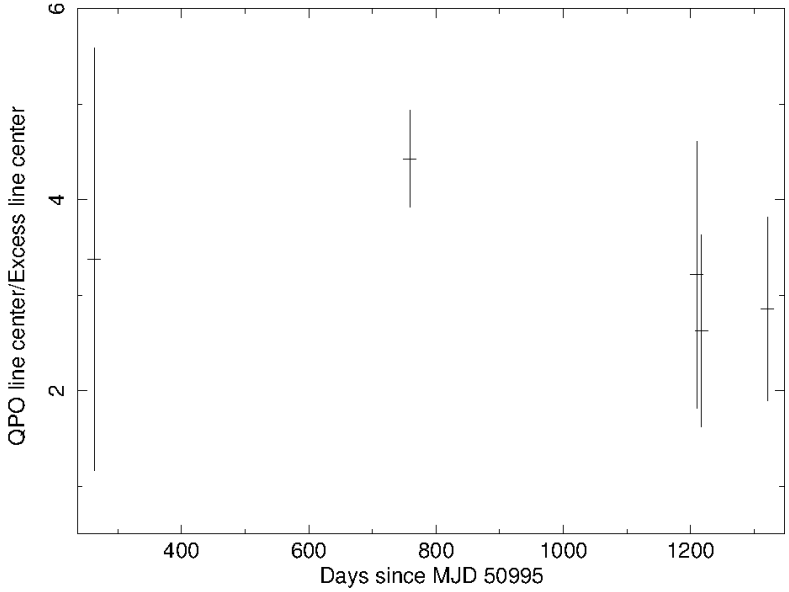

Figure 5.3: Line center ratio with respect to observation day.

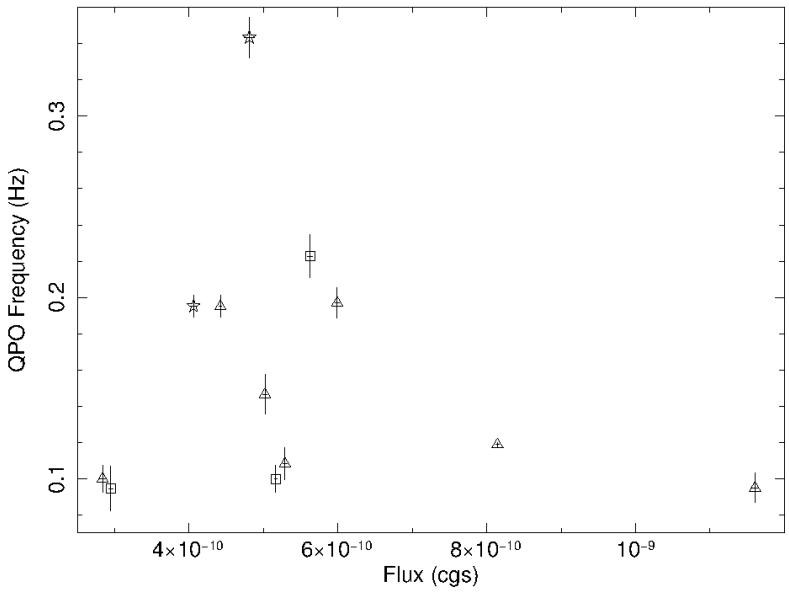

Figure 5.4: QPO frequency with respect to source X-ray flux. Stars are QPOs between 3-4σ detection, while triangles have significances between 2-3σ and squares have significances below 2σ.

frequencies at their relevant emission radii. At other times, the geometry of the binary and accretion do not allow higher frequencies to be seen by blocking the emission coming from these inner parts of the disk or these factors block the process generating these frequencies completely. Inevitably, stochastic variations of the Be star's stellar wind play a great role in this phenomenon. QPO centroid variability between flux values $4-6\times10^{-10}$ ergs/cm^2.s corresponds to QPOs in MJDs 51060, 51754, 52205, 52211, 52212, 52217, 52315 and 52316.

Therefore, below 4×10^{-10} ergs/cm^2.s or above 6×10^{-10} ergs/cm^2.s ,the emission somehow originates in a region that is able to produce a variety of QPO frequencies and outside this range, one cannot detect higher frequency QPOs. However,as will be mentioned, hardness of the source is more dominant in controlling QPO frequencies. In other words, the relationship of QPO centroid frequencies with flux is not as clear as their relationship with individual photon energies.

Seemingly there is no clear correlation between the excess line centers and the flux of the source. However, they seem to gather around $0.02-0.04$ Hz and above 0.07 Hz which could be further discussed with more data points. In this work, importance was given to the study of QPOs and not individual excess features that can be abundantly seen in power spectra of almost all observations. Here, only the excess values of power spectra which hosted QPOs and excess features simultaneously have been considered. A more detailed study on the broad noise structures appearing below 0.1 Hz can reveal more information about the nature of the noise features in X−Persei.

Figure (5.5) is the plot of ratio between QPO and Gaussian excess line centers versus source flux. Here, the ratio has a peak value at MJD 51754 and then gradually decreases as flux increases.

Line widths No correlation between QPO line center with respect to QPO line width and QPO line width with respect to time are observed. It is easily seen that regardless of the value of line center, widths of the Gaussian fits for the excess are close to 0.01 Hz. These width values show an overall increase in

values with time, which can be further evaluated by adding remaining excess values that were not seen with a simultaneous QPO. Line widths of the QPOs with respect to excess fits are pretty scattered and reveal no clear trend.

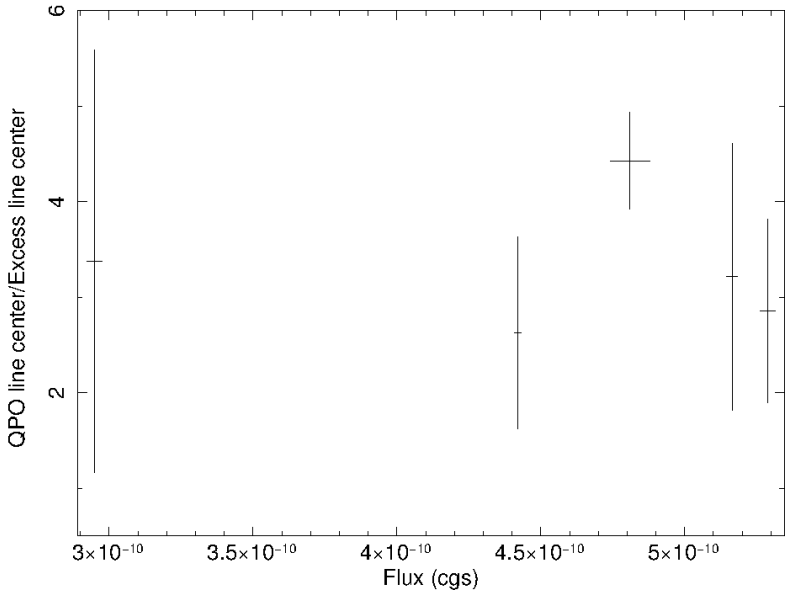

Figure 5.5: Line center ratio with respect to source X-ray flux.

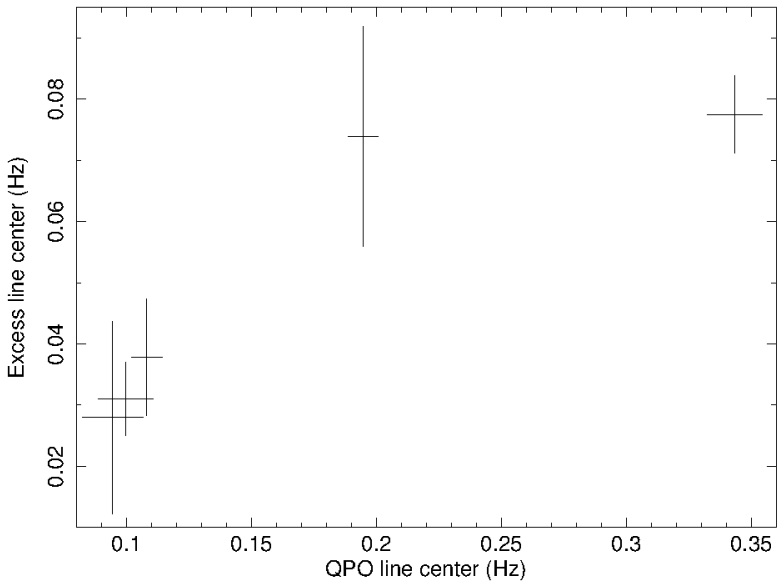

Figure 5.6: QPO line center with respect to excess line center.

Indices and RMS Amplitudes The relation between power spectral indices and noise parameters actually demonstrate the change in line centers of QPOs and power excess with the change of the hardness of emission coming from the source. Gaussian line centers versus double power law indices are much alike, there is a faint distinction between the behavior of line center versus first power law indice and the line center versus second power law indice. Smallest excess frequency has the smallest indice which gets higher as the frequency increases. This trend continues up to 0.04 Hz and there after, regardless of the excess frequency power, power law gets steeper again.

Since there are more data points in QPO frequencies to compare with relative indices of double power law continuum fit, the separation of frequencies in two distinct branches according to their power law indices are clear. It can be concluded that the mechanism responsible for QPO generation is active between ∼2-2.5 and between ∼0.5-0. Furthermore, there is no trend in QPO RMS amplitudes and their respective frequencies and no trend of QPO RMS amplitudes versus time is observed. On the other hand, as power excess line centers increase in frequency, it is seen that their respective RMS amplitudes grow as well.

Lastly, there is a clear correlation between the QPO and power excess line centers (Fig. 5.6). As QPO frequencies increase, excess frequencies tend to remain around a constant value, in contrast to their non-linear increase before 0.2 Hz.

Accretion disk of X-Persei Most of the Be type X-ray binaries have a highly unstable disk, going through erratic formation and dissipation even during small time intervals. For X-Persei, however, analysis of the QPO and outburst parameters indicate another possibility. RXTE data analysed for its timing properties in this work implies that 4U 0352+309 had an accretion disk from beginning to the end of the data, with outburst not causing this formation specifically. This is supported by the observation of 0.1-0.4 Hz QPOs at random times nearly throughout all the data and not just during the outburst. X-Persei shows spin-down until about 2.3×10^8 seconds from the start of observations, after which it reverses this trend and starts spinning up with the start of flaring activity (Acuner et al. 2014). Regular spin up and down behaviour in the period of the

neutron star is another sign of an accretion disk throughout the RXTE data. For quantitative investigation of the acretion disk, inner Keplerian disk radii have been estimated by making use of the QPO frequencies and source fluxes during individual observations. With the help of the detected QPO frequencies, below equation gives a constraint on the inner edge of the Keplerian disk,

$$r_0 = \left(\frac{GM}{4\pi^2}\right)^{1/3} \upsilon_k^{-2/3}. \tag{5.1}$$

where M is the neutron star mass which has a value of $1.4M\odot$. By making use of the relation,

$$r_0 \sim 0.52\mu^{4/7}(2GM)^{-1/7}\dot{M}^{-2/7} \tag{5.2}$$

magnetic dipole moment and hence the magnetic field of the pulsar can be estimated, where $\mu = B \times R^3$ is the magnetic dipole moment, R is the neutron star radius, taken as 10^6 cm and $\dot{M}$ is the mass accretion rate derived from Eqn. (2.6)(Ghosh & Lamb 1979). Alfvén radius is estimated from Eqn. (2.2) and source luminosity is calculated from the flux as,

$$L_x = 4\pi d^2 \times F_x \tag{5.3}$$

where F_x is the souce X−ray flux and d is the source distance taken as 950 pc. These values give the innermost boundary where QPOs are likely to be generated. This is an assumption in accordance with Keplerian and Beat Frequency models which imply that a QPO frequency is related to the Keplerian frequency at that particular radius where it is born. Therefore, it can be assumed that QPO frequencies are indeed generated by the Keplerian motions of matter from various radii inside the accretion disk. For all 12 QPOs, inner Keplerian disk radii, mass accretion rates, accretion luminosities, magnetic fields and magnetospheric radii have been estimated with the help of a basic Python script. The output can be seen in Table (5.1).

In this picture, it is highly possible that QPO and noise feature are generated by the interaction between Keplerian disk and the magnetic field of the neutron star.

Erratic variations in the visibility of QPO frequencies can be related the modification of the disk luminosity due to wind accretion. X-Per has a clear correlation

Table5.1: Some binary parameters for X-Persei derived from QPO frequency and flux values.

Epoch (MJD)	Source Luminosity (L_{34}) (ergs/s)	Mass accretion rate ($\dot{M}_{14}$) (g/s)	Keplerian inner disk radius (Rk_8) (cm)	Magnetic dipole moment(μ_{38}) (Gauss.m^3)	Magnetic field (B_{11}) (Gauss)	Magnetospheric radius (Rm_8) (cm)
51049	3.06	1.68	7.78	6.49	6.49	7.49
51060	4.31	2.41	4.99	3.56	3.56	4.80
51258	4.18	2.85	3.42	2.00	2.00	4.29
51754	5.19	2.85	3.42	2.00	2.00	3.29
52212	4.77	2.62	7.31	7.53	7.25	7.52
52217	6.47	3.55	4.95	4.27	4.27	4.76
52205	5.58	3.06	7.80	8.78	8.78	7.50
52211	6.07	3.34	4.56	3.59	3.59	4.39
52315	5.71	3.14	7.38	8.08	8.08	7.10
52316	5.42	2.98	6.03	5.52	5.52	5.80
52368	8.79	4.83	6.94	8.99	8.99	6.67
52687	14	7.71	8.06	14.8	14.8	7.75
Avg.	6.14×10^{34}	3.69×10^{14}	6.05×10^{8}	6.3×10^{29}	6.3×10^{11}	5.95×10^{8}

L_{34}, $\dot{M}_{14}$, Rk_8, μ_{29}, B_{11} and Rm_8 are in units of 10^{34}, 10^{14}, 10^8, 10^{29}, 10^{11} and 10^8 respectively.

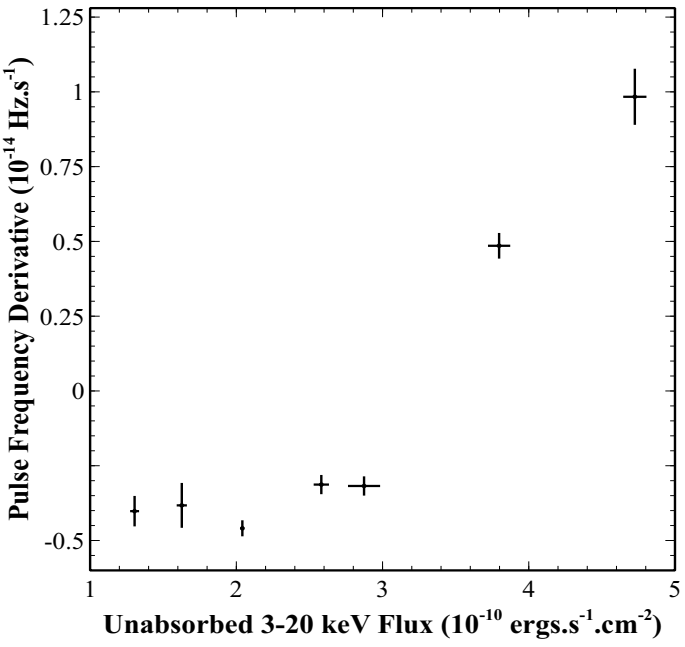

Figure 5.7: Pulse frequency derivatives with respect to unabsorbed flux (Acuner et al. 2014).

of $\dot{\omega}$ to $\dot{M}$. Source's pulse frequency derivatives are correlated with flux just as it is expected to be if it is a wind-accreting system with quasi−spherical accretion. Comparing Figure (2.12) with Figure (5.7) will give one a clear perspective.

These findings imply that X-Per is strongly wind driven and hence exhibits quasi−spherical accretion with occasional, although long lasting, disk formation eras which are revealed by the behaviour of pulse period derivaties and the existence of QPOs. This also explains the chaotic behaviour of the source, such as the lack of expected correlations among the flux and QPO frequency which is unlikely for HMXB QPO sources.

5.2 Broad-Band Power Spectra

Without being too constraining, it is suggested in this work that the constant trend at the lower frequencies f^0 reveal the band where there is no effect of either the disk or the magnetosphere, corresponding to a white noise component. First break at the spin frequency corresponds to the radius of corotation between the magnetosphere and the incoming material. After this break point, the power law follows f^{-1} and it is possible to observe the effects of both the accretion disk and the magnetosphere as well as their stochastic interactions between each other and the stellar wind of the Be companion. Since all of the QPO frequencies are observed after the second break, at the interval which has a power law trend of f^{-2}, we may assume that the disk extends up to and beyond 0.1 Hz in the frequency domain of power spectra.

The nature of broad band PDS of X−Persei suggests that it has at least two different accretion flow components dominating the overall flow. These breaks sometimes also correspond to different spectral states of sources if PDS is generated from data with a sufficiently long time interval (İçdem and Baykal 2011).

5.3 Hardness-Intensity and Color Diagrams

The most significant outcome of the hardness analysis is about the QPO generation regions. The highest QPO frequency can be observed while peeking at the regions/mechanisms which produce the softest photons. This might reveal further information about the nature of QPO generation mechanisms at the high energy photon generation regions and explain if it is really the case that these regions are not able to efficiently generate higher frequency QPOs as their soft photon emitting counterparts. Existence of a 0.34 Hz QPO during the dominance of soft energy photon generation mechanism/region and its occurance near the time of spin reversal may reveal details about the relationship between the torque applied to the source by the accreted material as well as its effect on the hardness and timing properties of the source.

Since the RXTE observations of X−Per cease near the peak of the outburst, no further remarks can be made about the rest of the flaring activity as well as the subsequent decay of the source luminosity and spectral properties during this time. Attempted hardness analysis of X−Per for this time era would be complete with the addition of suitable data spanning the decay of the outburst.

CHAPTER 6

CONCLUSION

In this thesis, RXTE observations of X-Persei/4U 0352+309 Be type X-ray binary system has been thoroughly analysed. RTXE archive hosts a total of 148 pointings amounting to 793 ks of observation time for X-Per. These observations spread between July 1998 and February 2003.

X-Persei is an X-ray source that has been carefully studied over the years since its initial detection in 1976 (White et al.1976). Although its timing properties are rather well-studied, no particular attention was paid to power spectral characteristics of the source except a short proceeding published by Takeshima in 1997.

This thesis is focused on the investigation of individual power spectra of small time intervals as well as the examination of characteristics of broader time spans. Mentioned investigations revealed the existence of quasi periodic variations principally observed around 0.1 to 0.4 Hz with significances varying between 1σ to greater than 3σ. Detection of QPOs suggests the existence of an accretion disk during the time period from 1998 to 2003. Observed QPO frequencies reveal a magnetic field of 6.3×10^{11} Gauss for the source. The magnetospheric radius corresponding to this magnetic field is $\sim 6 \times 10^{8}$ cm.

Hardness ratios derived from soft (3-7/7-10 keV) and hard (10-15/15-20 keV) energy bands reveal the relationship between the count rate and the hardness of X-Per during a gradual increase in X-ray luminosity. When the hardness-intensity and color diagrams in the soft energy band are investigated with re-

spect to time, it is seen that the relatively high energy photons emanating from the source initially become softer, which then start to harden steadily during this small outburst. It is remarkable that QPO frequencies ascend up to ~ 0.4 Hz during the time of the softest emission. In the hard energy band, no significant variability is observed. These spectral dependencies created the need of examining the energy spectra of the source as well. This examination has supported the argument that the soft X-ray emission mechanism is fruitful for QPO generation closer to the neutron star.

Besides narrow noise features, abundant broad power excesses at lower frequencies are striking in the PDS of the source. These dynamic structures fluctuate between 0.01-0.08 Hz in time. Due to the resistant nature of this activity throughout the data, it can be concluded that a particular accretion flow characteristic of X-Per is causing such a frequency dependent surplus in the X-ray emission. Further investigation of these structures together with the spectral and timing properties of X-Per might reveal interesting facts about the environment of accretion flow in BeXRBs.

REFERENCES

[1] Acuner Z., Inam S.Ç., Şahiner Ş., Serim M.M., Baykal A., Swank,J., 2014, in preparation.

[2] Alpar M. A., Shaham J., 1985, Nature, 317, 681.

[3] Angelini L. Recipes from the RXTE Cook Book. 17 January 2014. From http://heasarc.gsfc.nasa.gov/docs/xte/recipes/.

[4] Angelini L., Stella L., Parmar A.N., ApJ, 346, 906.

[5] Belloni T., Hasinger G., 1990, A&A, 230, 103.

[6] Bildsten L., Chakrabarty D., Chiu J., Finger M.H., Koh D.T., Nelson R.B., Prince T.A, Rubin B.C, Scott, D.M., Stollberg M., Vaughan, B.A., Wilson C.A., Wilson R.B., 1997, ApJ, 113, 367.

[7] Bjorkman J.E., Cassinelli J.P., 1993, ApJ, 409, 1, 429.

[8] Blondin J.M., Kallman T.R, Fryxell B.A., Taam R.E., 1990, ApJ, 356, 591.

[9] Brown J.C., Cassinelli J.P., Maheswaran M., 2008, ApJ, 688,2, 1320.

[10] Caballero I., Wilms J., 2012, Memorie della Societa Astronomica Italiana, 83, 230.

[11] Camero-Arranz A., Finger M.H., Wilson-Hodge C.A., Jenke P., Steele I., Coe M.J., Gutierrez-Soto J., Kretschmar P., Caballero I., Yan J., Rodríguez J., Suso J., Case G., Cherry M.L., Guiriec S., McBride V.A., 2012, ApJ, 754, 20, 906.

[12] Casares J., Negueruela I., Ribó M., Ribas I., Paredes J.M., Herrero A., Simón-Díaz S., Nature, 2014, 505, 7438, 378.

[13] Clark J.S., Tarasov A.E., Okazaki A.T., Roche P., Lyuty V.M., 2001, A&A, 380, 615.

[14] Cranmer S.R., 2009, ApJ, 701, 1, 396.

[15] Delgado-Marti H., Levine A.M., Pfahl E., Rappaport S.A., 2001, ApJ, 546, 455.

[16] Devasia J., James M., Paul B., Indulekha K.,2011, MNRAS, 414, 2, 1023.

[17] Dugair, M.R., Jaisawal G.K., Naik S., Jaaffrey S.N.A., 2013, MNRAS, 434, 3, 2458.

[18] Finger M.H., Wilson R.B., Harmon B.A., 1996, Apj, 459, 288.

[19] Finger M.H., 1998, AdSpR, 22, 7, 1007.

[20] Giacconi R., Gursky H., Paolini F.R., Rossi B.B., 1962, PRL, 9, 11, 439.

[21] Giacconi R., Gursky H., Kellog E., Schreier E., Tananbaum H., 1971, ApJ, 167, L67.

[22] Gilfanov M., Arefiev V., astro-ph, 0501215.

[23] Ghosh P., Pethick C.J., Lamb F.K., 1977, ApJ, 217, 578.

[24] Ghosh P., Lamb F.K., 1979, ApJ, 232, 259.

[25] Ghosh P., Lamb F.K., 1979, ApJ, 234, 296.

[26] Ghosh,L (2007). Rotation and Accretion Powered Pulsars. Singapore: World Scientific Publishing Co. Pte. Ltd.. 1-34.

[27] Icdem, B., Baykal, 2011, A&A, 529, A7.

[28] In't Zand J.J.M., Baykal A., Strohmayer T.E., 1998, ApJ, 496, 368.

[29] James M., Paul B., Devasia J., Indulekha K, 2010, MNRAS, 407, 285.

[30] Kaur R., Paul B., Raichur H., Sagar R., 2007, ApJ, 660, 2, 1409.

[31] Leahy D. A., Darbro W., Elsner R. F., Weisskopf M. C., Kahn S., Sutherland P. G., Grindlay J. E., 1983, ApJ, 266, 160.

[32] Lee U., Osaki Y., Saio H., 1991, MNRAS, 250, 432.

[33] Liu Q.Z., van Paradijs J., van den Heuvel E.P.J., 2005, A&A, 442, 3, 1135.

[34] Liu Q.Z., van Paradijs J., van den Heuvel E.P.J., 2006, A&A, 455, 3, 1165.

[35] Liu Q.Z., van Paradijs J., van den Heuvel E.P.J., 2007, A&A, 469, 3, 807.

[36] LOFT Assessment Study Report, 2013, ESA/SRE(2013)3.

[37] Lutovinov A., Tsygankov S., Chernyakova M., 2012, MNRAS, 423, 1978.

[38] Miyamoto S., Kimura K., Kitamoto S., Dotani T., Ebisawa K., 1991, ApJ, 383, 784.

[39] Monday D., Klein G., Lee S. The Assumptions of Anova. 15 February 2014. From $www.rohan.sdsu.edu/ \sim cdlin/677/ANOVA\_Assumptions.ppt$.

[40] Nagase F., 1989, PASJ, 41, 1.

[41] Okazaki A.T., 2001, PASJ, 53, 1, 119.

[42] Okazaki A.T., Negueruela I., 2000. The Be Phenomenon in Early-Type Stars. In IAU Colloquium 175, ASP Conference Proceedings, Vol. 214 (p.173). Myron A. Smith, Huib F. Henrichs (ED). Astronomical Society of the Pacific.

[43] Okazaki A.T., Negueruela I., 2001. X-ray Astronomy 2000. In ASP Conference Proceeding Vol. 234 (p281). Giacconi R., Serio S., Stella L. (ED). San Francisco: Astronomical Society of the Pacific.

[44] Okazaki A.T., Negueruela I., 2001, A&A, 377, 161.

[45] Paul B., Rao A.R., 1998. In Abstracts of the 19th Texas Symposium on Relativistic Astrophysics and Cosmology. Paul J., Montmerle T., Aubourg E. (ED). Meeting abstract.

[46] Porter J.M., 1998, A&A, 336, 966.

[47] Pringle J.E., 1996, MNRAS, 281, 1, 357

[48] Reig P, Belloni T., Israel G.L., Campana S., Gehrels N., Homan J., 2008, A&A, 485, 3, 797.

[49] Reig P., 2011, Ap&SS, 332, 1, 1.

[50] Reig P., Nespoli E., 2013, A&A, 551, A1.

[51] Revnivtsev M., Churazov E., Postnov K., Tsygankov S., 2009, A&A, 507, A94.

[52] Ryden B. Spherical Accretion. 20 January 2014. From $http : //www.astronomy.ohio - state.edu/ \sim ryden/ast825/ch8.pdf$.

[53] Shaham J., 1987.The origin and evolution of neutron stars. In Proceedings of the IAU Symposium,Nanjing, People's Republic of China (pp. 347-359). Dordrecht: D. Reidel Publishing Co.

[54] Shakura, N. I. and Sunyaev, R. A. 1973, A&A, 24, 337.

[55] Shakura N.I., Postnov K.A., Kochetkova A.Y., Hjalmarsdotter L., 2013, Physics Uspekhi, 56, 4, 321.

[56] Shapiro S.L., Lightman A.P., 1976, ApJ, 1, 555.

[57] Shirakawa A., Lai D., 2002, ApJ, 565, 1134.

[58] Shklovksy I.S., 1967, ApJ, 148, L1.

[59] Soong Y., Swank J.H., 1989. In ESA, The 23rd ESLAB Symposium on Two Topics in X Ray Astronomy. Volume 1: X Ray Binaries (pp.617-620).

[60] Stella L., Vietri M., Morsink S.M., 1999, ApJ, 524, L63.

[61] Takeshima T., Dotani T., Mitsuda K., Nagase F., 1994, ApJ, 436, 2, 871.

[62] Takeshima T., 1997, AAS 191, 111.04.

[63] Takeshima T., 1998. The Hot Universe. In Katsuji K., Shunji K., Masayuki I. (Ed), Proceedings of the IAU Symposium 188 (pp.368). Dordrecht: Kluwer Academic.

[64] Tananbaum H., Gursky H., Kellogg E. M., Levinson R., Schreier E., Giacconi R., 1972, ApJ, 174, L143.

[65] Van der Sluys M., 2014, De sterrenhemel voor Nederland en Belgie. 20 April 2014. From *http* : *//hemel.waarnemen.com/Informatie/Sterren/hoofdstuk*6.*htmlh*6.2.

[66] Van der Klis M., 1987. The origin and evolution of neutron stars. In Proceedings of the IAU Symposium,Nanjing, People's Republic of China (pp.321-330). Dordrecht: D. Reidel Publishing Co.

[67] Weisstein, Eric W. MathWorld, A Wolfram Web Resource. 30 March 2014. From http://mathworld.wolfram.com/Root-Mean-Square.html.

[68] White N.E., Mason K.E., Sanford P.W., Murdin P., 1976, MNRAS, 176, 20.

[69] Wilson C., Camero-Arranz A., Finger M.H., 2008, AAS, HEAD meeting, 10, 10.06.

APPENDIX A

POWER SPECTRA AND LIGHTCURVES

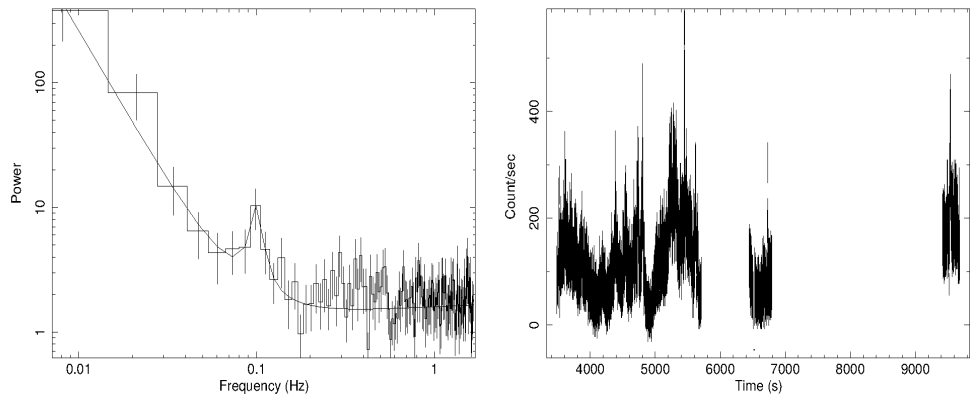

Figure A.1: PDS (left) and lightcurve (right) of MJD 51049.

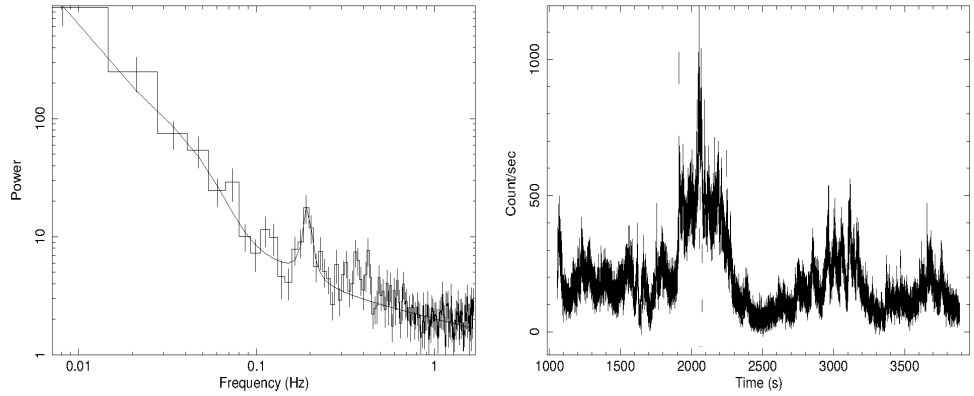

Figure A.2: PDS (left) and lightcurve (right) of MJD 51060.

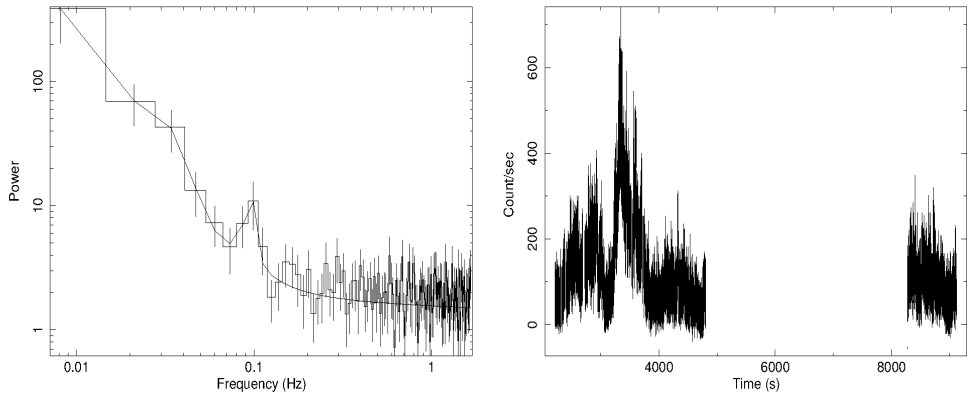

Figure A.3: PDS (left) and lightcurve (right) of MJD 51258.

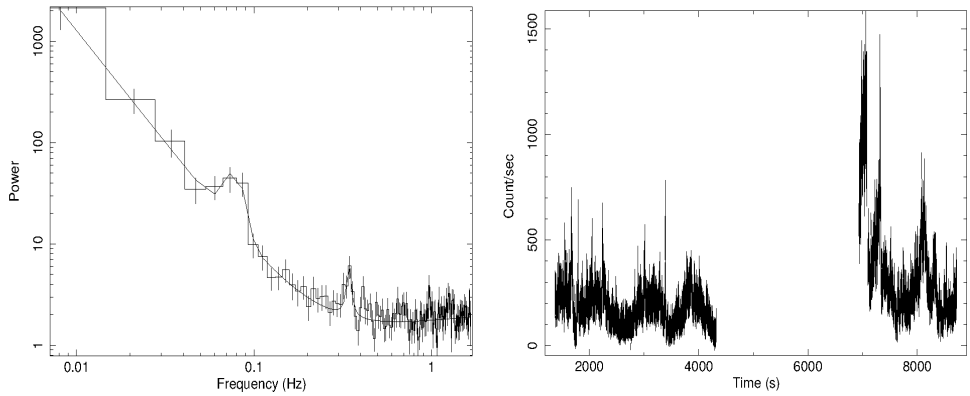

Figure A.4: PDS (left) and lightcurve (right) of MJD 51754.

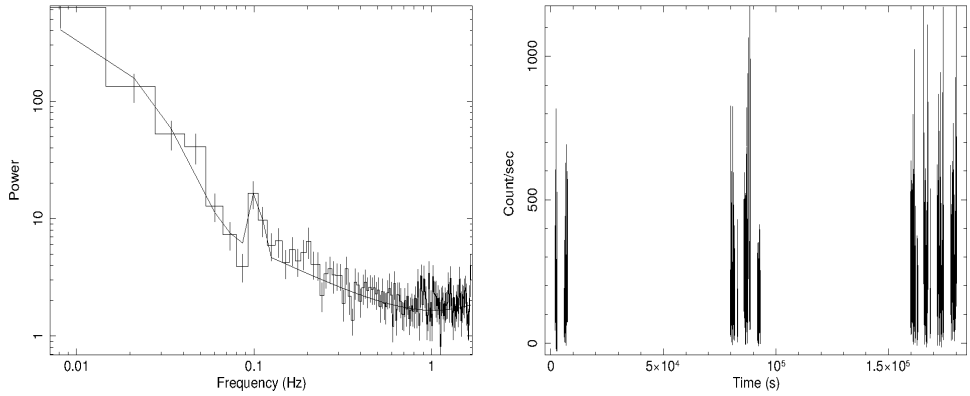

Figure A.5: PDS (left) and lightcurve (right) of MJD 52205.

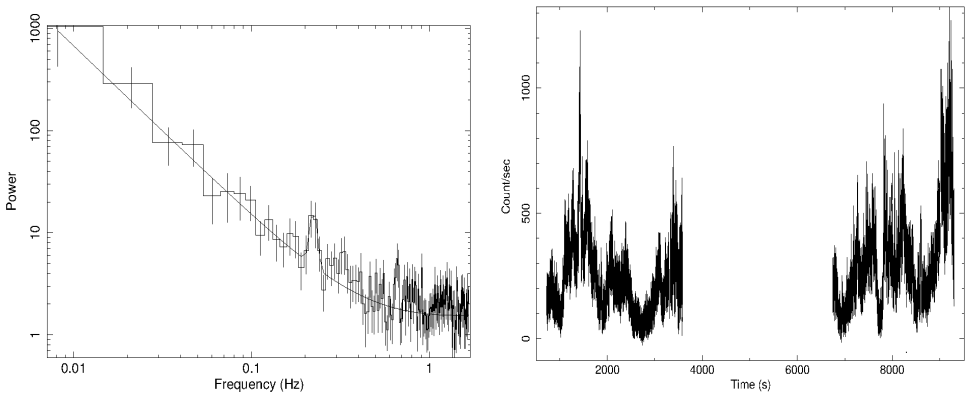

Figure A.6: PDS (left) and lightcurve (right) of MJD 52211.

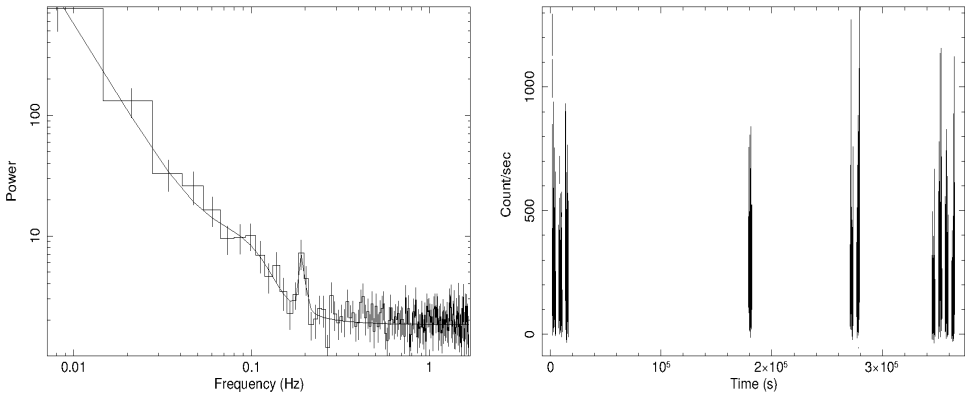

Figure A.7: PDS (left) and lightcurve (right) of MJD 52212.

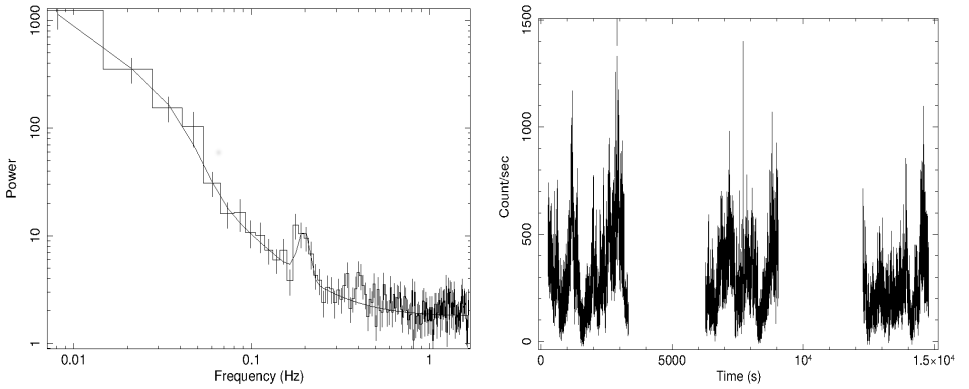

Figure A.8: PDS (left) and lightcurve (right) of MJD 52217.

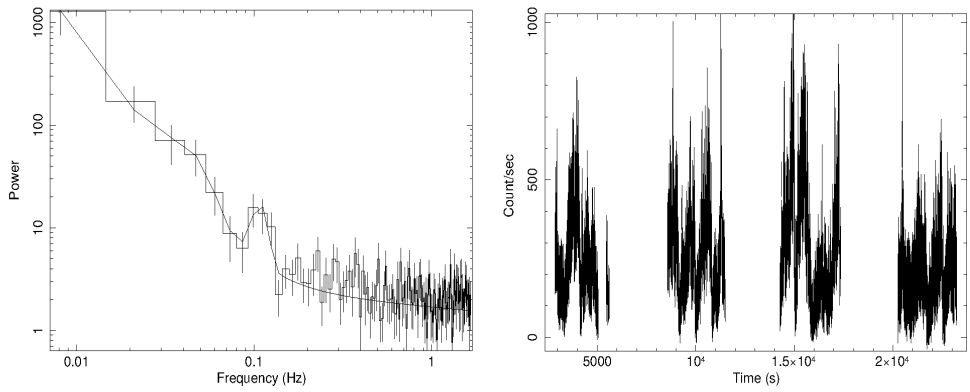

Figure A.9: PDS (left) and lightcurve (right) of MJD 52315.

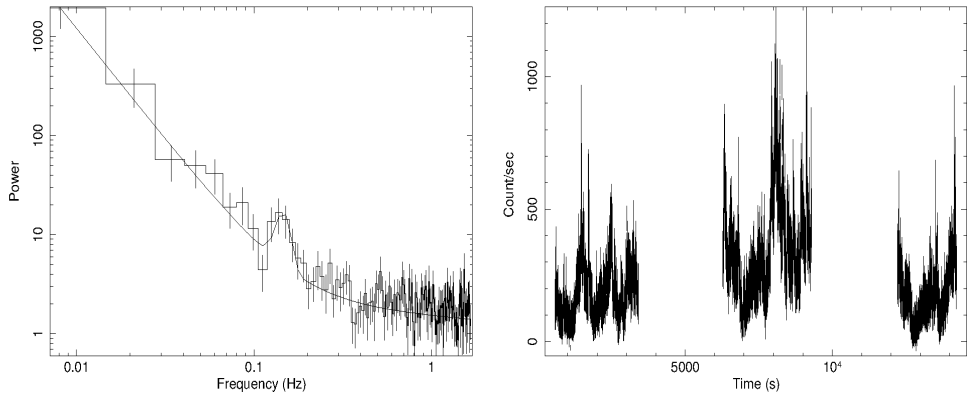

Figure A.10: PDS (left) and lightcurve (right) of MJD 52316.

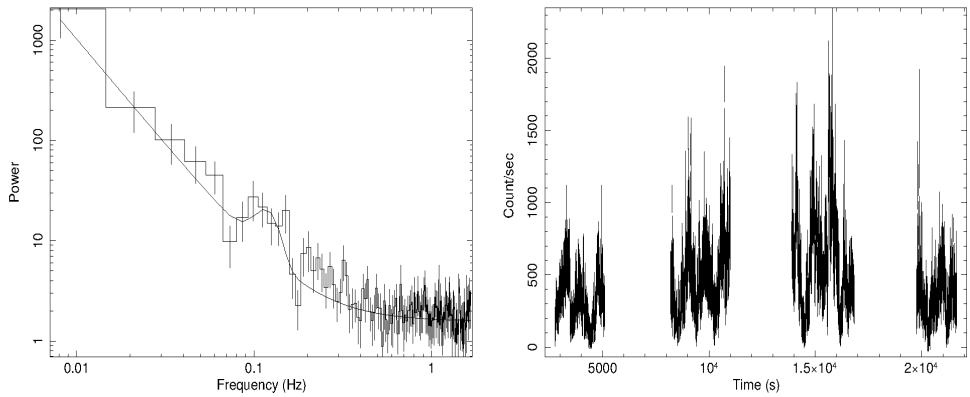

Figure A.11: PDS (left) and lightcurve (right) of MJD 52368.

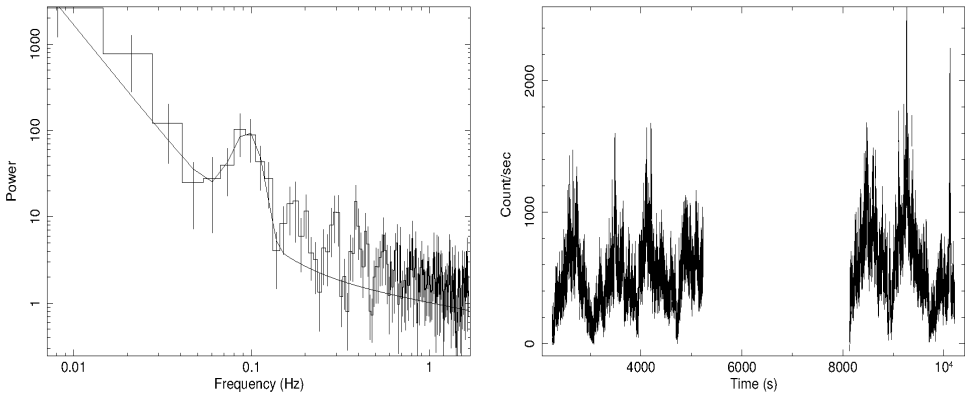

Figure A.12: PDS (left) and lightcurve (right) of MJD 52687.

APPENDIX B

HARD AND SOFT BAND LIGHTCURVES

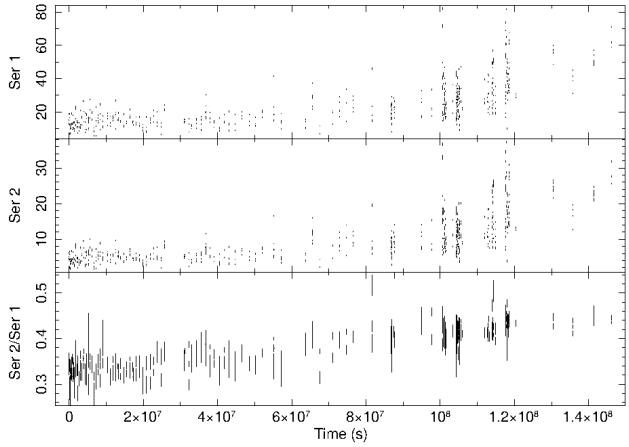

Figure B.1: Series ratio and intensity versus time diagrams for soft color (Series 1: 3-7 keV, Series 2: 7-10 keV).

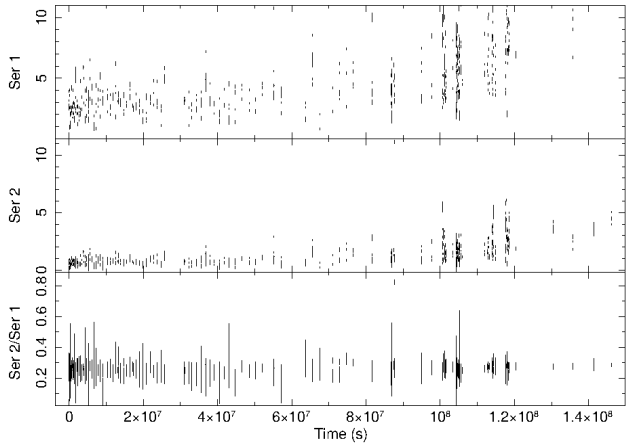

Figure B.2: Series ratio and intensity versus time diagrams for hard color (Series 1: 10-15 keV, Series 2: 15-20 keV).